contrast to the analogous reactions of CHD_3 (v_1 = 1) with F and O(^{3}P) atoms (*9*, *10*). In retrospect, this implication may not be too surprising. It has been demonstrated (*22*, *29*) that in the ground-state Cl + CHD_3 reaction, the product angular distribution essentially mirrors the opacity function (the reaction probability as a function of impact parameters) in a one-to-one correspondent manner [see figures 2 and 5 of (*22*)]. In accounting for enforcement of such a mirror-like correspondence, a rather weak anisotropic PES in the entrance valley could have been inferred. The structure of the transition state is product-like, and thus the reaction barrier is recessed in the exit valley. Upon vibrational excitation of CHD_3(v_1 = 1), the elongation of the C-H bond can enlarge the range of attack angles at the reaction barrier, thereby increasing the reaction probability at fixed impact parameters, but the resulting anisotropic interactions may not extend into the entrance valley far enough to appreciably steer the prealigned reagents.

References and Notes

1. F. F. Crim, *Proc. Natl. Acad. Sci. U.S.A.* **105**, 12654 (2008).
2. W. L. Hase, *Science* **266**, 998 (1994).
3. D. C. Clary, *Annu. Rev. Phys. Chem.* **41**, 61 (1990).
4. A. J. Orr-Ewing, R. N. Zare, *Annu. Rev. Phys. Chem.* **45**, 315 (1994).
5. D. Skouteris *et al.*, *Science* **286**, 1713 (1999).
6. R. D. Levine, *J. Phys. Chem.* **94**, 8872 (1990).
7. A. J. Alexander, M. Brouard, K. S. Kalogerakis, J. P. Simons, *Chem. Soc. Rev.* **27**, 405 (1998).
8. B. L. Yoder, R. Bisson, R. D. Beck, *Science* **329**, 553 (2010).
9. W. Zhang, H. Kawamata, K. Liu, *Science* **325**, 303 (2009).
10. F. Wang, K. Liu, *Chem. Sci.* **1**, 126 (2010).
11. G. Czakó, J. M. Bowman, *J. Am. Chem. Soc.* **131**, 17534 (2009).
12. The contrasting behaviors of O and F can also be qualitatively rationalized from the transition-state theory perspective. The transition state in F + CHD_3 possesses a reactant-like structure, and thus a stretched or compressed C-H bond of CHD_3 deviates from the transition-state structure, disfavoring the reaction. By contrast, ab initio calculations predicted that in O(^{3}P) + CHD_3, both the breaking C-H bond and forming O-H bond are elongated. Excitation of the C-H bond of CHD_3 therefore helps attain the transition-state structure.
13. W. R. Simpson, T. P. Rakitzis, S. A. Kandel, A. J. Orr-Ewing, R. N. Zare, *J. Chem. Phys.* **103**, 7313 (1995).
14. W. T. Duncan, T. N. Truong, *J. Chem. Phys.* **103**, 9642 (1995).
15. J. C. Corchado, D. G. Truhlar, J. Espinosa-Garcia, *J. Chem. Phys.* **112**, 9375 (2000).
16. S. Yan, Y.-T. Wu, B. Zhang, X.-F. Yue, K. Liu, *Science* **316**, 1723 (2007).
17. S. Yan, Y.-T. Wu, K. Liu, *Proc. Natl. Acad. Sci. U.S.A.* **105**, 12667 (2008).
18. J. J. Lin, J. Zhou, W. Shiu, K. Liu, *Rev. Sci. Instrum.* **74**, 2495 (2003).
19. J. J. Lin, J. Zhou, W. Shiu, K. Liu, *Science* **300**, 966 (2003).
20. O. N. Ulenikov *et al.*, *Mol. Phys.* **108**, 1209 (2010).
21. Magic angle imaging serves two purposes. First, at this polarization angle, the approaching Cl atom encounters a practically unpolarized CHD_3(v_1 = 1, j = 1) reagent. Previously, when we prepared CHD_3(v_1 = 1) in the source chamber (*16*, *17*), the excited reagents traveled for >100 μs before reacting, which we presumed was long enough to depolarize initially aligned CHD_3(v_1 = 1) molecules by hyperfine interactions. Indeed, the results from the acquired α_M image agree broadly with the previous findings. Second, the signals from the stretch-excited reagents under the three polarization angles are related by ($I_{//}$ + 2$I_{\perp}$) = 3Iα_M, which provides a stringent check (within ±1% in this work) of the consistency of the data.
22. G. Nyman, J. Zhou, B. Zhang, K. Liu, *Isr. J. Chem.* **47**, 1 (2007).
23. R. N. Zare, *Ber. Bunsenges. Phys. Chem* **86**, 422 (1982).
24. R. Altkorn, R. N. Zare, C. H. Greene, *Mol. Phys.* **55**, 1 (1985).
25. R. D. Levine, R. B. Bernstein, *Molecular Reaction Dynamics and Chemical Reactivity* (Oxford Univ. Press, Oxford, 1987).
26. In an optically aligned (not oriented) CHD_3 molecule, the H atom of the aligned C-H bond can point either toward or away from the approaching Cl atom; thus, no distinction of the head-versus-tail dynamics can be made.
27. In a direct reaction, the forward-scattered product is normally associated with large–impact parameter collisions, for which there is a purely kinematic smearing of the alignment effect even for a perfectly aligned reagent (*30*).
28. R. Martínez, M. González, P. Defazio, C. Petrongolo, *J. Chem. Phys.* **127**, 104302 (2007).
29. J. Zhou, B. Zhang, J. J. Lin, K. Liu, *Mol. Phys.* **103**, 1757 (2005).
30. I. Schetchter, R. D. Levine, *J. Chem. Soc. Faraday Trans. II* **85**, 1059 (1989).

31. We are indebted to S. Yan for earlier attempts of this project and to J. Lam for help with the experiment. This work was supported by National Science Council (NSC-99-2113-M-011-016), Academia Sinica, and the Air Force Office of Scientific Research (AOARD-10-4034).

Supporting Online Material

www.sciencemag.org/cgi/content/full/331/6019/900/DC1
Figs. S1 to S5
Tables S1 and S2
References

29 October 2010; accepted 13 January 2011
10.1126/science.1199771

The Magnitude and Duration of Late Ordovician–Early Silurian Glaciation

Seth Finnegan,[1]* Kristin Bergmann,[1] John M. Eiler,[1] David S. Jones,[2] David A. Fike,[2] Ian Eisenman,[1,3] Nigel C. Hughes,[4] Aradhna K. Tripati,[1,5] Woodward W. Fischer[1]

Understanding ancient climate changes is hampered by the inability to disentangle trends in ocean temperature from trends in continental ice volume. We used carbonate "clumped" isotope paleothermometry to constrain ocean temperatures, and thereby estimate ice volumes, through the Late Ordovician–Early Silurian glaciation. We find tropical ocean temperatures of 32° to 37°C except for short-lived cooling by ~5°C during the final Ordovician stage. Evidence for ice sheets spans much of the study interval, but the cooling pulse coincided with a glacial maximum during which ice volumes likely equaled or exceeded those of the last (Pleistocene) glacial maximum. This cooling also coincided with a large perturbation of the carbon cycle and the Late Ordovician mass extinction.

Earth history is punctuated by glacial episodes that vary widely in their magnitude and duration (*1*), as well as in their effects on global biodiversity (*2*). Far more is known about the most recent glacial age in the Pleistocene than about older glacial episodes. The Late Ordovician–Early Silurian glaciation of the southern supercontinent of Gondwana (Fig. 1A) is unusual because it occurred during a period when atmospheric partial pressure of CO_2 (pCO_2) was generally higher [perhaps 8 to 16 times higher (*3*)] than today's pCO_2, was short-lived compared to subsequent Gondwanan glaciations (*1*), and is the only glacial episode that appears to have coincided with a major mass extinction of marine life (*4*) (Fig. 1B). These observations have led to suggestions that the Late Ordovician–Early Silurian icehouse represents a climate mode distinct from more recent glaciations (*5*), but fundamental questions about the event are still largely unresolved: Estimates of peak ice sheet volume range from ~50 to more than 250 million km^3 (*6*) (Fig. 1A), estimates of its duration range from 35 million years (*1*) to less than 1 million years (*5*) (Fig. 1B), and it is unclear how much sea surface temperatures (SSTs) cooled in the tropical environments that hosted much of Late Ordovician biodiversity (*7*–*9*).

These uncertainties persist because few climate proxies can be reliably applied to Paleozoic rocks. Oxygen isotope ratios ($\delta^{18}O$) in well-preserved marine carbonate and phosphate minerals provide a useful proxy and have been widely applied in Paleozoic climate reconstruction (*5*, *7*, *8*) but suffer a fundamental limitation: The $\delta^{18}O$ value of a mineral is influenced by both the temperature and the isotopic composition of the water reservoir from which it precipitates ($\delta^{18}O_{water}$). Consequently, without independent constraints on one or the other of these variables, interpreting $\delta^{18}O$ trends in the stratigraphic record poses an underdetermined problem. This issue has been addressed for the Pleistocene last glacial maximum (LGM)—for example, using sediment porewater profiles (*10*)—but remains largely unresolved for older glaciations.

We used carbonate clumped isotope paleothermometry (*11*, *12*) to constrain the precipitation temperatures of a suite of Late Ordovician–Early Silurian carbonates. This approach measures the state of ordering of heavy isotopes (Δ_{47}) in carbonate minerals and is independent of the

[1]Division of Geological and Planetary Sciences, California Institute of Technology, Pasadena, CA 91125, USA. [2]Department of Earth and Planetary Sciences, Washington University, St. Louis, MO 63130, USA. [3]Department of Atmospheric Sciences, University of Washington, Seattle, WA 98195, USA. [4]Department of Earth Sciences, University of California, Riverside, CA 92521, USA. [5]Department of Earth and Space Sciences and Department of Atmospheric and Oceanic Sciences, Institute of Geophysics and Planetary Physics, University of California, Los Angeles, CA 90095, USA.

*To whom correspondence should be addressed. E-mail: sethf@caltech.edu

isotopic composition of water from which the minerals grew. Combination of this approach with conventional carbonate-water oxygen isotope paleothermometry thus provides a means for untangling trends in reservoir composition from those in temperature. To minimize the effects of burial diagenesis, we examined exceptionally fossiliferous and well-studied successions in the U.S. midcontinent and on Anticosti Island, Québec, Canada (*13*) (Fig. 1A and fig. S1), which have experienced relatively little sedimentary burial. To assay the quality of our proxy measurements, we sampled fossils from several taxonomic groups and surrounding sediments from a broad range of lithotypes and across a large range of preservation states to characterize diagenesis and vital effects (*13*) (figs. S2 and S3).

There is no evidence of a systematic burial overprint on Δ_{47} values in our data set. Similar ranges are recorded in the Vauréal Formation and the Jupiter Formation (Fig. 2A) (*12*) despite ~500 m of intervening strata in the Anticosti Basin (fig. S1). The highest Δ_{47} values (lowest temperatures) on Anticosti are not observed in the stratigraphically highest samples but rather in samples from the middle of the stratigraphic column. To confirm that Δ_{47} does capture known postdepositional thermal gradients, we sampled micritic carbonates from the Vauréal Formation that are intruded by a Jurassic-aged dike. Δ_{47} values immediately adjacent to the dike are the lowest in our entire data set, corresponding to precipitation temperatures exceeding 230°C, but inferred temperatures fall to 39°C within 14 m of the dike-country rock contact (fig. S4).

Δ_{47} values of skeletal carbonates range from 0.631 to 0.501 (Fig. 2 and table S1), corresponding to a temperature range from 28° to 64°C. This range implies a mixture of plausibly primary and diagenetically altered phases, the latter being typically depleted in both Δ_{47} and $\delta^{18}O$ (fig. S5). Because diagenetic recrystallization of calcite tends to deplete Sr and enrich Mn and Fe (*14*, *15*), we evaluated concentrations of these metals in a large and representative subset of our samples (*13*) (figs. S6 to S8). Most samples fall within the "well-preserved" compositional range identified by previous studies (fig. S6), but there is a strong relationship between the first principal component (PC1) of trace metal concentrations and Δ_{47}: High PC1 values (low Sr and high Mn and Fe, fig. S7) are associated with higher precipitation temperatures and in many cases with textural evidence of diagenetic alteration (Fig. 2B). The highest Δ_{47} value and lowest PC1 value associated with texturally altered samples are 0.589 and –0.285, respectively. We therefore excluded all samples that fall outside this range from our reconstructions of ocean temperature and chemistry (Fig. 2B). We included samples that were not evaluated for trace metal concentration but that have Δ_{47} values higher than 0.589, but similar trends result if these samples are also excluded (fig. S9). Even the best-preserved samples likely contain small amounts of dispersed recrystallized phases that cannot easily be avoided given the large sample sizes required for adequately precise measurement of Δ_{47}. Our temperature reconstructions should therefore be viewed as maximal SST estimates, and we base trend lines on the lowest-temperature samples from each stratigraphic interval.

Reconstructed temperatures are nearly indistinguishable from each other and consistent with a narrow range from 32° to 37°C throughout most of the ~20 million years covered by our time series (Fig. 3A). SSTs in this range rarely occur in the modern tropics, but a variety of proxies record similar temperatures during Mesozoic–early Cenozoic greenhouse intervals (*16*–*18*), during which atmospheric pCO_2 is inferred in some reconstructions to have exceeded five times present atmospheric levels (*3*). Temperatures below this range (28° to 31°C) occur only in samples from the Laframboise Member of the Ellis Bay Formation on Anticosti Island. This Hirnantian-aged unit (*13*) records a major drop in sea level (*19*, *20*) and a large positive carbon isotope excursion (*19*); both are recognized globally in other sedimentary successions (*4*, *20*). The best preserved of these successions also record exceptionally enriched $\delta^{18}O$ values [–2 per mil (‰) to 0‰ Vienna Pee Dee belemnite (VPDB)] during Hirnantian time (*8*, *20*, *21*), as do our Laframboise Member samples (Fig. 3B and table S1). $\delta^{18}O$ values preceding and following the Hirnantian peak are lighter but still enriched relative to the ~–5‰ (VPDB) baseline values that characterize the beginning and end of the time series (Fig. 3B). Well-preserved brachiopods and trilobites could not be extracted from the Laframboise Member, and hence our data from the Hirnantian maximum are derived exclusively from rugose corals. Δ_{47} is not known to be subject to disequilibrium vital effects among modern taxa (*11*), but such effects cannot be ruled out and there remains uncertainty regarding the possibility of a vital effect on $\delta^{18}O$ in rugose corals (*13*). However, our Hirnantian $\delta^{18}O$ values are similar to those recorded by brachiopods in contemporaneous sections (*5*, *8*, *20*, *21*), and the

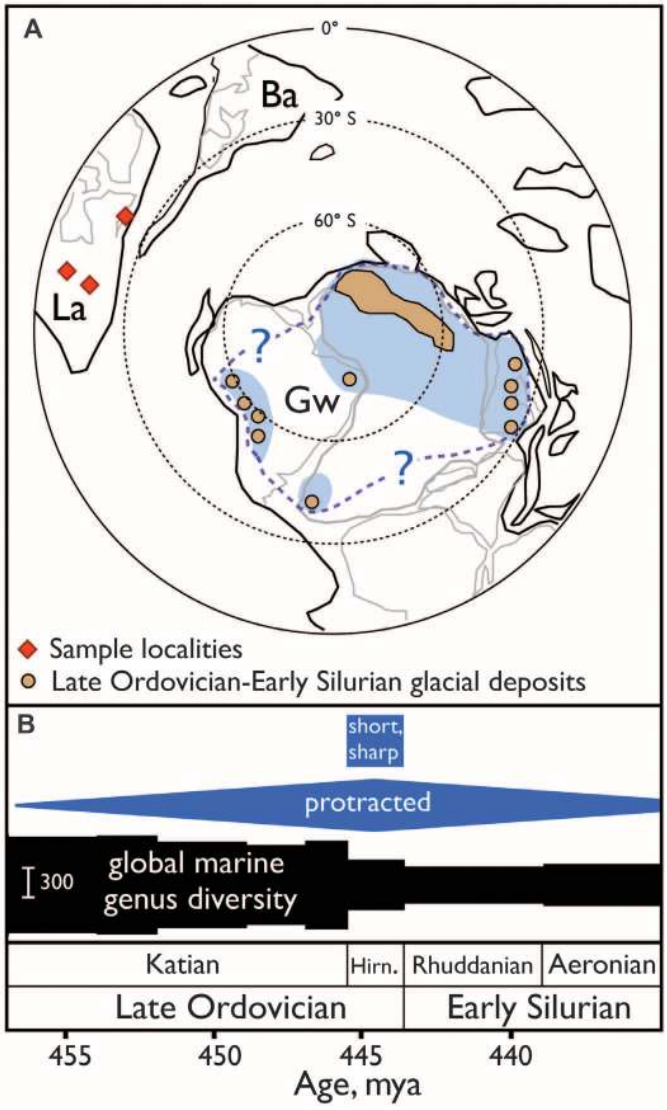

Fig. 1. (**A**) South polar view of a simplified Late Ordovician paleogeographic reconstruction (*27*), indicating the positions of Late Ordovician to Early Silurian–aged glacial deposits in Gondwana (Gw, tan solid circles and areas) and of the Laurentian (La) localities sampled for this study (red diamonds). Ba indicates Baltica. Two possible reconstructions of the Gondwanan ice sheet (*6*) are shown: a minimal, discontinuous reconstruction (light blue shading) and a maximal continent-spanning reconstruction (dashed blue outline). (**B**) Hypotheses regarding the duration of the icehouse interval: short and sharp, restricted largely or entirely to the Hirnantian (Hirn.) stage lasting as little as 500,000 years (*5*), and protracted, with a peak in the Hirnantian interval (*1*, *28*). Marine invertebrate genus diversity (black spindle) (*29*) declined both at the beginning and at the end of the Hirnantian stage. mya, million years ago.

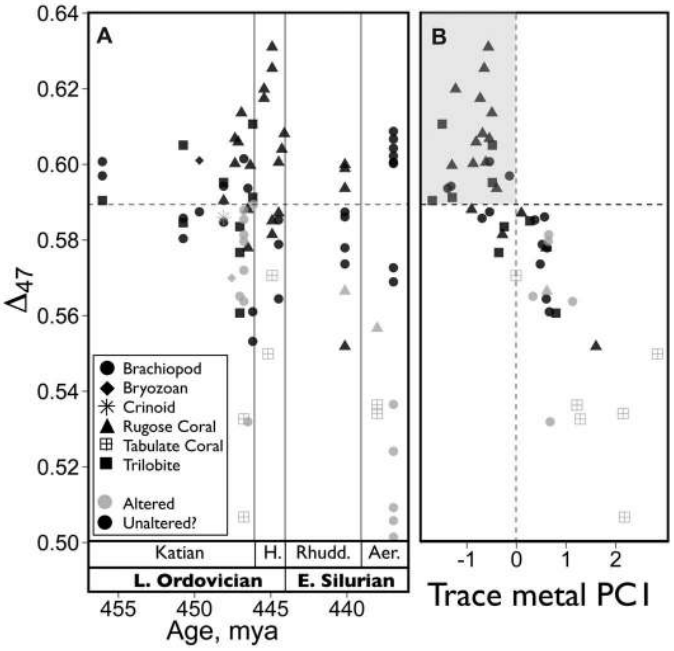

Fig. 2. (**A**) Δ_{47} values of all samples examined for this study, keyed to taxonomic group and preservation state, and plotted against stratigraphic position. (**B**) PC1 of log-transformed Mn, Fe, and Sr concentrations for a large subset ($n = 52$) of the samples shown in (A). PC1 explains 86% of variation in trace metal composition and receives strong positive loading from Mn and Fe and weak negative loading from Sr. Dashed lines indicate PC1 and Δ_{47} cutoffs for inclusion (shaded region) in paleoclimate reconstructions; H, Hirnantian; Rhudd, Rhuddanian; Aer, Aeronian. Ages within stages are interpolated on the basis of stratigraphic position.

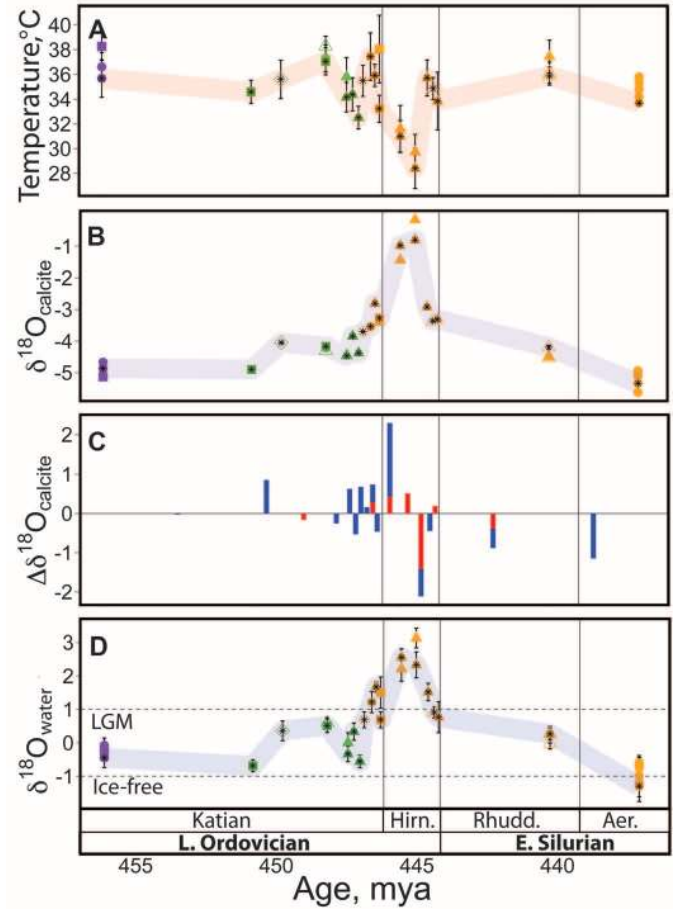

Fig. 3. Symbols as in Fig. 2; color indicates provenance: purple, Upper Mississippi Valley; green, Cincinnati Arch; orange, Anticosti Island. Solid symbols indicate samples selected on the basis of both trace metal concentration and Δ_{47} criteria; open symbols indicate samples selected based only on Δ_{47} value. Error bars on individual samples (*13*) are ± 1 SE ($\delta^{18}O$ errors are smaller than symbols) and reflect analytical precision for samples analyzed once and reproducibility for samples analyzed multiple times (table S1). Samples marked by asterisks are the lowest-temperature samples in their respective time intervals and are the basis for trendlines. (**A**) Δ_{47}-derived near-surface ocean temperature trend for the early Katian to late Aeronian interval. (**B**) $\delta^{18}O$ (VPDB) trend over the same interval. (**C**) Relative contributions of temperature and $\delta^{18}O_{water}$ to changes in $\delta^{18}O$ ($\Delta\delta^{18}O$) between successive time intervals. Bars are scaled to the magnitude of $\Delta\delta^{18}O$, and color proportion is scaled to the relative contribution of temperature change (red) and change in the oxygen isotopic composition of seawater (blue) to $\Delta\delta^{18}O$. (**D**) $\delta^{18}O_{water}$ (VSMOW) trend. Dotted lines indicate $\delta^{18}O_{water}$ value during the Pleistocene LGM (*10*) and expected $\delta^{18}O_{water}$ value for an ice-free world.

Hirnantian excursion can be defined by using only rugose corals (fig. S10) and thus cannot be explained by systematic differences between rugose corals and other taxa.

Our Δ_{47} measurements place independent constraints on how much of the temporal variation in $\delta^{18}O$ can be explained by temperature changes, with the remainder attributable to changes in the isotopic composition of seawater. For much of the study interval, $\delta^{18}O$ variation is driven almost entirely by changes in $\delta^{18}O_{water}$ (Fig. 3C); only during Hirnantian time can changes in temperature account for a substantial proportion of this variation.

$\delta^{18}O_{water}$ estimates (Fig. 3D) fall between –1‰ Vienna standard mean ocean water (VSMOW), the value expected for an ice-free world (*22*), and 1‰, the value of LGM seawater (*10*), for most of the study interval. However, $\delta^{18}O_{water}$ estimates exceed 2‰ during the Hirnantian glacial maximum. Assuming (i) the $\delta^{18}O$ trend reflects changes in mean ocean water, (ii) the $\delta^{18}O$ of all surface reservoirs combined has been unchanged from the Late Ordovician to the recent (*13*), and (iii) the $\delta^{18}O$ of glacial ice was comparable to the LGM, these values imply that continental ice volumes during the Hirnantian maximum substantially exceeded those of the LGM (fig. S11). The mean isotopic composition of Late Ordovician glacial ice cannot be directly measured, but inferred Hirnantian ice volumes exceed those of the LGM for any mean ice value heavier than –60‰, approaching the most depleted values observed in the present day (fig. S11).

$\delta^{18}O_{water}$ trends suggest multiple episodes of moderate glaciation and deglaciation throughout the mid-late Katian interval, with little evidence of substantial ice sheets before this time (Fig. 3D). The most enriched $\delta^{18}O_{water}$ values before the Hirnantian peak come from the sub-Laframboise Ellis Bay Formation, the age of which has been controversial (*13*). Assigning this unit an early Hirnantian rather than latest Katian age would restrict $\delta^{18}O_{water}$ values higher than 1‰ to Hirnantian time (fig. S12), but multiple mid-late Katian samples > 0‰ still indicate the development of substantial pre-Hirnantian ice sheets, at least transiently. Relatively high $\delta^{18}O_{water}$ values also occur in latest Hirnantian samples from the lowermost Becscie Formation, which records a sharp rise in sea level and waning of the Hirnantian carbon isotope excursion. These observations reveal that latest Ordovician sea level rise represents only partial deglaciation of Gondwana. $\delta^{18}O_{water}$ values consistent with moderate ice sheets persist for several million years, returning to near –1‰ by the end of the Aeronian Stage (Fig. 3D).

Our results imply that initial glaciation of Gondwana occurred with little or no cooling of the tropical oceans, that tropical SSTs exceeded the present-day range except during the Hirnantian glacial maximum, and that they warmed rapidly after the Hirnantian maximum despite the persistence of substantial continental ice volumes for several million years. This contrasts with

previous work using classical oxygen isotope paleothermometry on conodont apatite from Anticosti and elsewhere (*7*) that reconstructed temperatures in the modern SST range for much of the Late Ordovician–Early Silurian except for cooling to ~24°C below and above the Laframboise Member (*7*). These estimates assumed a constant $\delta^{18}O_{water}$ of –1.0‰; substituting our $\delta^{18}O_{water}$ values from the same units raises inferred temperatures by, on average, 8°C. Recent revision of the phosphate-water oxygen isotope fractionation equation (*23*) further suggests that all conodont-derived temperature estimates should be revised upward, bringing them into the range that we observe for the Late Ordovician–Early Silurian.

We cannot rule out the possibility that the trends we observe are influenced by changes in the basin hydrology of the Taconic Foreland, but, if they accurately reflect global trends in the tropical oceans, they imply a nonlinear relationship between tropical ocean temperatures and continental ice volumes (fig. S13A). This contrasts with expectations from climate simulations using a modern continental configuration and from proxy records of the past 60 million years (*13*) (fig. S13, B and C). Furthermore, coexistence of substantial south polar ice sheets with tropical SSTs regionally in excess of 30°C implies a steeper meridional temperature gradient than during other major glacial episodes (*12*, *24*). Minor glaciations inferred to have occurred under high CO_2 conditions in the late Mesozoic–early Cenozoic (*16*, *25*) may have exhibited similar gradients but were comparatively short-lived. Both of these observations could plausibly be explained by nonlinear changes in the intensity of oceanic meridional overturning circulation (*26*), similar to those previously invoked to explain changes in the behavior of the Hirnantian carbon cycle (*4*, *5*, *20*). Although speculative, some support for this hypothesis is provided by the coincidence of our observed cooling pulse with the globally recognized Hirnantian positive carbon isotope excursion (*5*, *19*, *20*).

Lastly, by demonstrating that tropical cooling was largely limited to the Hirnantian Stage, our results support hypotheses linking the two-pulsed nature of the Late Ordovician mass extinction to rapid climate changes at the beginning and end of this interval (*4*, *20*).

References and Notes

1. L. A. Frakes, J. E. Francis, J. I. Syktus, *Climate Modes of the Phanerozoic* (Cambridge Univ. Press, Cambridge, 1996).
2. A. Raymond, C. Metz, *J. Geol.* **112**, 655 (2004).
3. R. A. Berner, *Geochim. Cosmochim. Acta* **70**, 5653 (2006).
4. P. M. Sheehan, *Annu. Rev. Earth Planet. Sci.* **29**, 331 (2001).
5. P. J. Brenchley *et al.*, *Geology* **22**, 295 (1994).
6. D. P. Le Heron, J. A. Dowdeswell, *J. Geol. Soc. London* **166**, 277 (2009).
7. J. A. Trotter, I. S. Williams, C. R. Barnes, C. Lécuyer, R. S. Nicoll, *Science* **321**, 550 (2008).
8. J. D. Marshall, P. D. Middleton, *J. Geol. Soc. London* **147**, 1 (1990).
9. A. D. Herrmann, M. E. Patzkowsky, D. Pollard, *Palaeogeogr. Palaeoclimatol. Palaeoecol.* **206**, 59 (2004).
10. D. P. Schrag *et al.*, *Quat. Sci. Rev.* **21**, 331 (2002).
11. P. Ghosh *et al.*, *Geochim. Cosmochim. Acta* **70**, 1439 (2006).
12. R. E. Came *et al.*, *Nature* **449**, 198 (2007).
13. Materials and methods are available as supporting material on *Science* Online.
14. U. Brand, J. Veizer, *J. Sediment. Res.* **50**, 1219 (1981).
15. G. A. Shields *et al.*, *Geochim. Cosmochim. Acta* **67**, 2005 (2003).
16. A. Bornemann *et al.*, *Science* **319**, 189 (2008).
17. S. Schouten *et al.*, *Geology* **31**, 1069 (2003).
18. P. N. Pearson *et al.*, *Nature* **413**, 481 (2001).
19. A. Desrochers, C. Farley, A. Achab, E. Asselin, J. F. Riva, *Palaeogeogr. Palaeoclimatol. Palaeoecol.* **296**, 248 (2010).
20. P. J. Brenchley *et al.*, *Geol. Soc. Am. Bull.* **115**, 89 (2003).
21. L. Hints *et al.*, *Est. J. Earth Sci.* **59**, 1 (2010).
22. S. M. Savin, *Annu. Rev. Earth Planet. Sci.* **5**, 319 (1977).
23. E. Pucéat *et al.*, *Earth Planet. Sci. Lett.* **298**, 135 (2010).
24. MARGO Project Members, *Nat. Geosci.* **2**, 127 (2009).
25. A. Tripati, J. Backman, H. Elderfield, P. Ferretti, *Nature* **436**, 341 (2005).
26. R. J. Stouffer, S. Manabe, *Clim. Dyn.* **20**, 759 (2003).
27. L. R. M. Cocks, T. H. Torsvik, *J. Geol. Soc. London* **159**, 631 (2002).
28. M. R. Saltzman, S. A. Young, *Geology* **33**, 109 (2005).
29. J. J. Sepkoski Jr., *Bull. Am. Paleontol.* **363**, 560 (2002).

30. We thank T. Raub, M. Rohrssen, and B. Gaines for assistance with field and lab work; D. Boulet and Société des établissements de plein air du Québec (SEPAQ) Anticosti for permission to work in Anticosti National Park; and B. Hunda for supplying samples. This work was funded by an Agouron Institute award to W.W.F. and D.A.F. and NSF Division of Earth Sciences awards to W.W.F. and J.M.E.

Supporting Online Material

www.sciencemag.org/cgi/content/full/science.1200803/DC1
Materials and Methods
Figs. S1 to S13
Table S1
References

23 November 2010; accepted 19 January 2011
Published online 27 January 2011;
10.1126/science.1200803

Hibernation in Black Bears: Independence of Metabolic Suppression from Body Temperature

Øivind Tøien,[1]* John Blake,[1] Dale M. Edgar,[2]† Dennis A. Grahn,[3] H. Craig Heller,[3] Brian M. Barnes[1]*

Black bears hibernate for 5 to 7 months a year and, during this time, do not eat, drink, urinate, or defecate. We measured metabolic rate and body temperature in hibernating black bears and found that they suppress metabolism to 25% of basal rates while regulating body temperature from 30° to 36°C, in multiday cycles. Heart rates were reduced from 55 to as few as 9 beats per minute, with profound sinus arrhythmia. After returning to normal body temperature and emerging from dens, bears maintained a reduced metabolic rate for up to 3 weeks. The pronounced reduction and delayed recovery of metabolic rate in hibernating bears suggest that the majority of metabolic suppression during hibernation is independent of lowered body temperature.

Mammalian hibernation is well characterized in species such as marmots, ground squirrels, bats, and dasyurid marsupials (*1*). These small (<5 kg) hibernators undergo regulated decreases in core body temperature (T_b) to near or below freezing during torpor bouts that last days to weeks (*2*–*5*). Torpor is periodically interrupted by arousals to normothermia (35° to 38°C) that usually last for less than one day (*6*, *7*). During torpor, metabolic rates of small hibernators decrease to 2 to 5% of basal metabolic rate (BMR) (*8*–*10*). However, the relative contributions of temperature-dependent (described by Q_{10}, rate coefficient for a 10°C change in T_b) and temperature-independent mechanisms of metabolic suppression depend on the size of animals and stage of entry into torpor (*11*). In contrast, the relationships between T_b and metabolism in the large hibernators of the bear family Ursidae have remained unknown because technical limitations have prevented continuous, long-term monitoring in these 30 to 200 kg or larger animals. We used telemetry and respirometry to record T_b, metabolic rates, and heartbeat patterns of black bears, *Ursus americanus*, through their hibernation and post-hibernation recovery.

Black bears were nuisance animals captured in south-central or interior Alaska in late autumn 3 different years and transported to facilities at the Institute of Arctic Biology, University of Alaska Fairbanks. Radio transmitters for T_b and electromyogram (EMG)/electrocardiogram (ECG) were surgically implanted (*12*), and animals were transferred to outdoor enclosures in an isolated wooded area. Bears hibernated inside 0.8 m^3 wooden nest boxes with straw for bedding and equipped with infrared cameras, activity detectors, and telemetry-receiving antennas. Food and water were not provided. Air was continuously collected from the closed hibernacula to record O_2 consumption (a measure of metabolic rate). After

[1]Institute of Arctic Biology, University of Alaska Fairbanks, Fairbanks, AK 99775, USA. [2]Department of Psychiatry and Behavioral Sciences, School of Medicine, Stanford University, CA 94305, USA. [3]Department of Biological Sciences, Stanford University, CA 94305, USA.

*To whom correspondence should be addressed. E-mail: otoien@alaska.edu (O.T.); bmbarnes@alaska.edu (B.M.B.)
†Present address: Lilly Research Centre, Eli Lilly, Windlesham, Surrey, GU20 6PH, UK.

www.sciencemag.org/cgi/content/full/science.1200803/DC1

Supporting Online Material for

The Magnitude and Duration of Late Ordovician–Early Silurian Glaciation

Seth Finnegan,* Kristin Bergmann, John M. Eiler, David S. Jones, David A. Fike, Ian Eisenman, Nigel C. Hughes, Aradhna K. Tripati, Woodward W. Fischer

*To whom correspondence should be addressed. E-mail: sethf@caltech.edu

Published 27 January 2010 on *Science* Express
DOI: 10.1126/science.1200803

This PDF file includes:

Supporting Online Material

Contents:

A. Geologic setting

All samples were collected from Laurentia (core North America). Late Katian-Aeronian samples come from the exceptionally complete and fossiliferous record of Anticosti Island in the Gulf of St. Lawrence, Québec (*S1-S4*) and early-late Katian samples come from two classic and well-described cratonic successions in the U.S. midcontinent (upper Mississippi Valley of IA-WI-MN-IL (*S5, S6*) and Cincinnati Arch of OH-KY-IN (*S7-S10*); (Fig S1). Laurentia was rotated ~45° clockwise from its current orientation and straddled the equator during Late Ordovician and Early Silurian time (*S11, S12*), and all of the sampled units were located in continental shelf and epicontinental seaways within tropical latitudes.

Sedimentation in the Anticosti Basin began in Late Cambrian time and subsidence and sedimentation rates reached a Middle to Late Ordovician maximum due to crustal loading associated with thrust sheets from the advance of the Taconic Arc (*S13-S15*). Subsidence continued into the Early Silurian, finally waning with the maturation of Taconic mountain building near the end of Early Silurian time (*S15*). Similar to contemporaneous sections elsewhere, the Anticosti Basin shows evidence of a dramatic shallowing of sea level in the latest Ordovician Hirnantian Stage (*S3, S4, S16-S19*). However, perhaps because of the relatively high rates of subsidence and sediment accumulation, it is one of the few Late Ordovician depocenters in Laurentia where sedimentation continued through Hirnantian time without a major nonconformity (*S20*). Minor nonconformities are present, however (*S4*), and there is controversy regarding how much of Hirnantian time is represented in the section and whether this is apportioned to the entire Ellis Bay Formation or only to the very condensed uppermost (Laframboise) member of the Ellis Bay Formation and the lowermost portion of the overlying Becscie Formation(see "Age assignments" below).

Hirnantian-aged sediments are thin, discontinuous, and largely unfossiliferous in the upper Mississippi Valley (*S21, S22*) and are entirely absent on the Cincinnati Arch (*S9, S22*). However, these successions also contain strata considerably older than those exposed at the surface on Anticosti. Both the upper Mississippi Valley and Cincinnati Arch successions were deposited on the flanks of persistent basement highs (The Kankakee Arch, formed by subsidence in the adjacent Michigan and Illinois Basins (*S23*), and the Cincinnati Arch, a forebulge associated with the Taconic Orogeny (*S8, S23*)). Consequently, they are thinner and less deeply buried than coeval successions in adjacent cratonic and foreland basins. Paleozoic sedimentation in the upper Mississippi Valley ceased in Silurian time, and the total preserved thickness of post-Ordovician sediments is, in most places, << 100 m (*S23*). Sedimentation continued into the Mississippian on the flanks of the Cincinnati Arch, such that the preserved thickness of post-Ordovician sediments in this region ranges from 0 in southern Ohio and central Kentucky to >500 m in east-central and west-central Kentucky (*S23*). Although more than three km of sediments accumulated in the Anticosti Basin (*S24*),only the upper third of this package is exposed at the surface[4]. Hence even the stratigraphically lowest exposed sediments, the upper portion of the late Katian Vauréal Formation, are thought to

have experienced < 1 km of post-depositional burial (though the possibility that Late Silurian-Devonian sediments were deposited but have been eroded away cannot be discounted (S*13, S25, S26*)).

B. Age assignments

We assigned ages to samples based primarily on the stages indicated for formations by Bergstrom et al., 2010 (*S27*), Buggisch et al. 2010 (*S28*), Long, 2007 (*S15*), and Achab et al., 2010 (S*1*). Where multiple samples from a formation or set of formations falling within a single stage are included, we interpolated ages, where possible, based on relative stratigraphic position. For samples from multiple localities that could not be correlated at sub-stage resolution, we assigned them all the same age. Samples from the Elkhorn Formation and the lowermost Becscie Formation were ordered based on their $\delta^{13}C$ values, with reference to the $\delta^{13}C$ curves published by Bergstrom et al., 2010 (*S27*), and Desrochers et al. (*S4*). Correlation between the Katian sequences on Anticosti and in the Cincinnati Arch region is based on the assignment of both the youngest Ordovician unit the Cincinnati Arch region (Elkhorn Formation) and the oldest exposed unit on Anticosti (lower Vauréal Formation) to the D. *complanatus* graptolite zone (*S1, S27*).

There is uncertainty regarding the precise age of the lower Ellis Bay Formation. Carbon isotopic evidence suggests that only the Laframboise Member and the overlying lowermost Becscie Formation are Hirnantian in age, with the underlying members of the Ellis Bay Formation usually regarded as of Latest Katian age (*S20*). Although the lower Ellis Bay Formation is richly fossiliferous, relatively few age-diagnostic taxa have been recovered from it (*S20*), and multiple hypotheses persist over the identity and biostratigraphic utility of these taxa. We follow Bergstrom et al., 2006 (*S29*) and Kaljo et al., 2008 (*S31*) in placing the base of the Hirnantian near the base of the Laframboise Member, but others have suggested that all or most of the Ellis Bay Formation is in fact of Hirnantian age (*S1, S3, S4, S31-S33*). Using this alternative age model to construct our time series (Fig. S12) does not change our inferences about the magnitude or overall duration of glaciation, but would confine $\delta^{18}O_{water}$ values exceeding 1‰ to the Hirnantian Stage.

C. Constraints on calcification depth

All three of the sample basins represent storm-influenced mixed carbonate-clastic ramp-platform depositional settings above storm wave base (*S4, S6, S17, S34-S37*). Limiting the bathymetric range of sampling is important because pelagic calcified organisms were largely absent from early Paleozoic oceans, and the calcitic taxa available for geochemical analyses were benthic. Restricting our analyses to these units ensures estimates of the chemistry and temperature of the relatively homogenous upper ~100 meters of a well-mixed water column. The shallowest depositional environment in the Anticosti sequence is represented by the Laframboise Member of the Ellis Bay Formation, which records a large and globally recognized eustatic regression (*S3, S19, S38*). The fact that this unit shows evidence of dramatic cooling, rather than the slightly higher temperatures that should be associated with shallowing in the absence of any

climate change, argues strongly against a major role for depth changes in driving observed temperature trends.

D. Collection and preparation of samples

Samples from the Vauréal, Ellis Bay, Becscie, Merrimack, and Gun River Formations (Fig. S1) were collected by SF, WWF, DSJ, and DAF during fieldwork on Anticosti Island in June and July of 2009. Sample localities and coordinates are given in table S1; measured stratigraphic sections and additional locality information are available upon request. Samples from the Jupiter Formation and their Δ_{47} and bulk isotope values previously described in Came et al., 2007 (*S38*). Samples from the Decorah Formation were collected at Wang's Corner, MN by KB in the summer of 2009. Samples from the Kope, Bellevue and Waynesville formations of the Cincinnati Arch region were collected by SF and KB in the summer of 2010, with additional samples from the Kope, Waynesville, Whitewater and Elkhorn formations graciously provided by Brenda Hunda from the collections of the Cincinnati Museum of Natural History. Samples were collected from a variety of lithofacies, but focused where possible on shales from which individual fossils could be manually separated. Slabs of cemented wackestone-packstone beds with well-preserved fossils and mud drapes on the upper surface were also collected in localities from which individual fossils could not be freed from the matrix. Fossils were manually flaked from the surfaces of these slabs using a dental pick. For brachiopods, this flaking focused on the secondary prismatic calcite layer to minimize matrix contamination (*S39-S41*). In addition, several *in-situ* tabulate coral colonies were collected from lime mudstone-dominate units. Following initial preparation to remove them from the matrix all samples were sonicated for 2 hours to remove residual matrix material; nevertheless this material could not always be completely removed and the presence of variable amounts of residual matrix material containing late-stage diagenetic carbonate phases likely accounts for many of the samples that give relatively high (38-45° C) Δ_{47} temperatures and have altered trace metal signatures despite pristine textures (Table S1). Following sonification, samples were either powdered with a mortar and pestle (trilobite and brachiopod material) or microrotary drill (rugose and tabulate corals). Some whole-rock slabs were also drilled to obtain matrix micrites for comparison with fossils. Only the apical ends of rugose corals were drilled, following removal of the outermost layer of skeletal material with an abrasive bit, to avoid the matrix and secondary cements commonly found within the calice. Tabulate corals, all of which preserved clear textural evidence of post-depositional alteration, were sampled in multiple spots to evaluate Δ_{47} gradients associated with the amount of recrystallization and/or post-depositional void filling by diagenetic cements.

E. Δ_{47} analysis and standardization

Approximately 10 mg of powder was used for each measurement; some samples were measured as much as 5 times to reduce analytical uncertainty and to evaluate sample heterogeneity. CO_2 was extracted from powders by phosphoric acid digestion at 90° C following the standard procedures outlined in Ghosh et al., 2006 (*S42*). Extracted CO_2

was analyzed on a Finnigan MAT253 gas source mass spectrometer configured to collect in the mass-44 to mass-49 range. The sample gas and a reference gas were analyzed 8 times each (8 acquisitions) in the course of each measurement. $\delta^{18}O$ and $\delta^{13}C$ were measured along with δ_{47} for each acquisition. Acquisition-to-acquisition standard deviations were on average 0.03 for δ_{47}, 0.04‰ for $\delta^{18}O$, and 0.02‰ for $\delta^{13}C$. Three isotopologues contribute to the mass-47 ion beam ($^{18}O^{13}C^{16}O$, $^{17}O^{12}C^{18}O$ and $^{17}O^{13}C^{17}O$) but the signal is dominated by the abundance of $^{18}O^{13}C^{16}O$ due to the rarity of ^{17}O. Variations in the mass-47/mass-44 ratio (R^{47}) are converted to Δ_{47} by comparing them to CO_2 gases of known $\delta^{18}O$ and $\delta^{13}C$ composition that were heated to 1000° C for two hours to achieve a stochastic R^{47} value for that composition. Δ_{47} is defined as the ‰ difference between the R^{47} value measured for a given sample and the R^{47} value that would be expected for that sample if its stable carbon and oxygen isotopes were randomly distributed among all possible isotopologues. Heated gases of three different known compositions were used to minimize uncertainty in the Δ_{47} standardization, and standardization of each sample was based only heated gases analyzed in the week prior to its analysis.

Δ_{47} values were converted to carbonate growth temperature estimates based on the relationship (*S42*):

$$\Delta_{47} = 50.0592(10^6\ T^{-2})-0.02$$

where T is temperature in degrees Kelvin.

F. Determination of $\delta^{18}O_{water}$

Determination of $\delta^{18}O_{water}$ is based on the low-temperature inorganic calcite fractionation equation of Kim and O'Neil, 1997 (*S43*):

$$1000\ln\alpha\sim(\text{Calcite-}H_20) = 18.03\ (\ 10^3T^{-1}) - 32.42$$

G. Estimating ice volumes from $\delta^{18}O_{water}$

For converting $\delta^{18}O_{water}$ to ice volume estimates we assume that the $\delta^{18}O_{water}$ value in an ice-free world would be ~-1.0 as estimated by Savin, 1977 (*S44*) , and we assume that the total volume of all surface water reservoirs has remained constant at 1,403,120,000 km^3. The major uncertainty in this calculation is the assumption of mean oxygen isotopic composition of glacial ice ($\delta^{18}O_{ice}$) in the Late Ordovician-Early Silurian, a quantity that is not measurable from the rock record. To accommodate this we calculated inferred ice volumes for a given $\delta^{18}O_{water}$ value assuming multiple values for $\delta^{18}O_{ice}$ (Fig. S11). If the Gondwanan ice sheets had a mean $\delta^{18}O_{ice}$ values similar to that of the last glacial maximum (~-40‰, a weighted average that assumes a value of -30‰ for the now-vanished Laurentide ice sheet(S*46*) and values of -30‰ and -55‰, respectively, for remaining ice sheets in Greenland and Antarctica), observed Hirnantian $\delta^{18}O_{water}$ values imply ice volumes exceeding the estimated 84,000,000 km^3 (*S46, S47*) present during the LGM. Only for $\delta^{18}O_{ice}$ values lighter than -60‰ do observed Hirnantian $\delta^{18}O_{water}$ values

imply ice volumes lower than those of the LGM. Because ~-60‰ is the close to the most extreme depletion observed in snow anywhere in the present day (*S48*) we regard it as unlikely that the mean $\delta^{18}O_{ice}$ of the Gondwanan ice sheet was this isotopically light. Consequently the Hirnantian glacial maximum was likely characterized by very large ice volumes, substantially higher than the LGM.

Our use of -1.0‰ as an ice-free baseline assumes that the O^{18}/O^{16} ratio of the oceans has not changed since the Ordovician, but our arguments about trends in ice volume are not tied to this assumption; we would reconstruct a similar relative ice volume trajectory for any assumed ice-free baseline value. Although weathering inputs and hydrothermal exchange processes may influence the oxygen isotopic composition of seawater (*S49*), the residence time of oxygen isotopes in the ocean with respect to these processes is much longer than the duration of the reconstructed $\delta^{18}O_{water}$ excursion.

H. Trace elemental analysis

A large and representative subset of samples (54 in total, 51 of which are skeletal carbonates) were analyzed for concentrations of Sr, Mn, and Fe using inductively coupled plasma atomic emission spectroscopy. Sample powders were dissolved in weak nitric acid. Standards for Sr, Fe, and Mn were prepared in nitric acid of the same concentration to minimize matrix effects. Sample and standard solutions were run on a Thermo iCAP 6300 radial view ICP-OES, using a Cetac ASX 260 autosampler with solutions aspirated to the Ar plasma using a peristaltic pump. Three standard solutions (blank, 1 ppm, and 10 ppm) were run between every multiple of 10 sample unknowns. Reproducibility is better than 5%, assessed by multiple runs of known standard concentrations.

I. Assessing post-depositional alteration of proxy ($\delta^{18}O$, Δ_{47}) signals

All Paleozoic carbonate successions have undergone episodes of diagenesis and, in many cases, metamorphism. Because clumped isotope paleothermometry records aspects of the solid state ordering of isotopologues, it is sensitive to post-depositional recrystallization: original calcitic phases can be partially or entirely replaced by new phases that record ambient (geothermal) temperatures at depth. Applying this proxy to estimate ancient temperatures depends on selecting fossil material that has been minimally impacted by diagenesis. In this section we provide a discussion of the observations, field tests, techniques, and criteria we used to assess and understand the effects of post-depositional alteration.

Dike test

One way of determining the quality of clumped isotope temperature estimates is to examine the trend of the proxy across expected gradients in post-depositional alteration. A section of the Vauréal Formation at Falaise de Puyjalons is bisected by an 8 m thick Jurassic-aged quartz-tholeiitic dike (*S50*). Samples (collected by T. Raub) taken from 0.70, 4.95, and 13.35 meters from the contact with the dike, display the expected thermal gradient of decreasing temperature with greater distance from the intrusion. A total

temperature differential of 180° C is observed in this field test (Fig. S4a), with temperatures falling from 219° C near the dike to 39° C – suggestive of original ocean temperatures with a relatively mild diagenetic overprint – 13.35 meters away from the contact. $\delta^{18}O_{calcite}$ shows the opposite trend increasing by ~4‰ over the same interval (Fig. S4b), suggesting that the alteration during contact heating with the dike occurred in the presence of a meteoric aquifer.

Textural analysis

We used light microscopy to examine the textural details and preservation state of all samples, and scanning electron microscopy to examine a representative subset consisting of 20 samples (Fig. S2). Most of the brachiopod and trilobite material examined shows apparently excellent preservation with well-defined calcitic prisms clearly visible and little evidence of recrystallization or secondary precipitation (Fig. S2a-d). Still, some of these samples have trace metal compositions suggestive of moderate diagenetic alteration and low Δ_{47} values indicative of relatively high crystallization temperatures (Figs. S6-S8, Table S1). In some cases, particularly for samples that were manually flaked from strongly lithified limestone slabs, it is clear that this reflects a variable admixture of micritic matrix material and secondary cements that could not be removed from the fossils. In most cases, however, it is not clear whether it represents matrix contamination or cryptic recrystallization/secondary precipitation within the skeletal material. Tabulate corals, by contrast, always preserve clear textural evidence of pervasive recrystallization and secondary void-filling calcite precipitation (Fig. S2e-f). These samples also tend to return strongly positive (altered) scores on trace metal composition PC 1 and low Δ_{47} values corresponding to crystallization temperatures ranging from 43 to 62° C. Rugose corals often show a range of preservation states within a single corallite (Figs S2g-i, S3) with prominent diagenetic alteration fronts and secondary calcite phases a common feature (Figs S2i, S3). We avoided individuals, such as that shown in Fig S2i, that appeared to be pervasively altered in extensive regions. More commonly, diagenetic fronts are limited to discrete regions around the periphery of the corallite (Fig. S2g, S3) and can be easily avoided even at the relatively coarse sampling scale dictated by our material requirements.

Trace element composition

Both theory and empirical patterns suggest that diagenetic stabilization of calcite tends to drive increases in the concentration of Mn and Fe and decreases in the concentration of Sr (*S39, S51-S55*). Our dataset provides support for this view from comparing concentrations of these elements to Δ_{47} values (Fig. 2, Fig. S6a-c; Table S1). Mn and Fe show strong negative correlations, indicating increasing concentration at higher crystallization temperatures, and Sr shows a weak positive correlation with Δ_{47}. We used a principal components analysis (PCA) of log-transformed Sr, Mn, and Fe abundances to summarize this information in a single eigenvector (PC 1, which receives strong positive loadings from Mn and Fe and weak negative loading from Sr and explains 86% of the variance in log trace metal concentrations among the 51 samples). PC 1 is strongly correlated with Δ_{47} (Fig. S6d), but the relationship is not linear, showing a pronounced

step between 0.580 and 0.590 above which there is no apparent association between the two variables. Because trace metal systematics vary among the taxa included here it is somewhat reductive to include all samples in a single principal components analysis. Hence, we also did separate PCA analyses of trace metal composition for brachiopods, for rugose corals, and for trilobites. All three groups show evidence of a similar relationship between trace metal composition and Δ_{47} (Fig. S7).

Comparisons among co-occurring phases

Selecting the least-altered samples depends on understanding the direction (with respect to Δ_{47} and bulk isotopic composition) of diagenetic alteration vector trajectories. One approach to characterizing alteration trajectories is to compare co-occurring phases that precipitated in a known sequence based on petrographic relations. (for example, skeletal material versus void-filling spar or enclosing sediment). Five such comparisons are shown in fig. S5; in each case the later phase is lighter in $\delta^{18}O$ and precipitated at higher temperature than the earlier (skeletal) phase. This does not mean that skeletal phases are unaltered, as the temperatures indicated for some suggest very substantial contamination by secondary phases (fig. S5). However, it allows us to characterize the trajectory of diagenetic alteration and to establish that in all of the units thus evaluated diagenesis is largely driven by interaction with relatively high-temperature and ^{18}O-depleted fluids.

This provides a framework for determining which samples have been most affected by diagenetic alteration when multiple samples from the same stratigraphic horizon are compared. Such comparisons support a primary origin for the Hirnantian $\delta^{18}O$ excursion. For example, of four rugose corals analyzed from horizon 901-12, two give relatively low temperatures (901-12-RC1, 30°C, and 901-12-RC2, 30°C) and two give relatively high temperatures (901-12-RC3, 40°C, and 901-12-LRC, 40°C). The former are isotopically heavy ($\delta^{13}C$ = 4.06, 4.47, $\delta^{18}O$ = -0.80, -0.16), whereas the latter are relatively depleted ($\delta^{13}C$ = 3.11, 3.70, $\delta^{18}O$ = -3.17, -3.13). Therefore either the hotter samples have been altered by interaction with warm and isotopically light fluids or the colder samples have been altered by interaction with cold and isotopically heavy fluids. Low-temperature fluids ($\leq$ 30°C in order to have produced observed Δ_{47} temperatures) must occur very close to the surface, and hence would generally be expected to have a strong meteoric influence and be isotopically light with respect to oxygen and carbon.

Even if a realistic alteration scenario involving low-temperature but isotopically heavy fluids could be envisioned, our data do not support such a model. The expectation, were this the case, would be that within the Laframboise Member the most altered materials would be isotopically heaviest and the least altered materials would be isotopically lightest. In fact, we observe the opposite pattern. For example, the skeletal material of sample 901-10-RC1 (a rugose coral) has a Δ_{47} temperature of 31°C, $\delta^{13}C$ of 4.18, and $\delta^{18}O$ of -0.97, whereas the enclosing sediment has a Δ_{47} temperature of 35°C, $\delta^{13}C$ of 3.33, and $\delta^{18}O$ of -3.02 (Figs. S3, S5)-much more similar to the values observed in the relatively high-temperature skeletal material from samples 901-12-RC3 and 901-12-LRC, and also characteristic, in terms of $\delta^{13}C$ and $\delta^{18}O$, of whole-rock values for this section.

Consequently, it is extremely difficult to explain the Hirnantian excursion (which is similar to that seen in other sections, see below) as a diagenetic artifact.

Comparison with published data

Comparison with previously published results from other sections provides a way of checking whether the proxy values we observe are plausibly primary. With the exception of one previous paper (*S38*) (the results of which are included in our dataset) no other Δ_{47}.data are available for Late Ordovician-Early Silurian fossils or sediments. However, we can compare our $\delta^{18}O$ data with several published studies from Anticosti and from other regions. Within the Hirnantian Laframboise Member of the Ellis Bay Formation, we observe $\delta^{18}O$ values in skeletal carbonates ranging from -4.59 to -0.16 (VPDB). Samples that appear to be strongly altered based on trace metal and Δ_{47} data (see criteria in next section) have values ranging from -4.59 to -3.13, whereas those that appear to be less altered have values ranging from -1.44 to -0.16. The former values are similar to those observed in whole-rock analyses of Hirnantian sediments from Anticosti (*S56*) and the Baltic (*S57*), whereas the latter values are in the same range as the heaviest values reported from well-preserved Hirnantian brachiopods in Baltic sections (*S19, S58, S59*). A single brachiopod analyzed from the interval of the $\delta^{13}C$ excursion in the Laframboise Member attains a value (~-2‰) intermediate between these ranges (*S19*), but the other two examined for this analysis (*S19*) had $\delta^{18}O$ values similar to whole-rock values for this section, raising the possibility that all three may be compromised. Taken as a whole, these observations suggest that the heavy $\delta^{18}O$ values we observe are capturing a primary signal and reinforce our interpretation and that of others that the lighter values in whole-rock samples (and in the altered corals) reflect a diagenetic overprint. It should also be noted that the best-preserved $\delta^{18}O$ values we observe from before and after the Hirnantian excursion, are also similar to previously published $\delta^{18}O$ values from these time-intervals (S*19, S58-S63*), as is the magnitude of the excursion relative to this baseline.

J. Within-bed variability and potential vital effects

The influence of disequilibrium „vital' effects on the Δ_{47} system appears to be relatively minor among extant taxa (*S42, S64*), but vital effects on $\delta^{18}O$ are widespread among both modern and ancient taxa. There is particular uncertainty in this area with regard to rugose corals; these are an important part of our dataset because they are the only well-preserved taxon that could be extracted from the Laframboise Member. Relatively little is known about whether rugose corals exhibit vital effects similar to those of modern scleractinian corals (to which they were not closely related). Brand (*S53, S65*) found that the best-preserved rugose corals in the Pennsylvanian Kendrick Fauna (KY) were on average ~5‰ lighter in $\delta^{18}O$ than co-occurring brachiopods, and ascribed this to a vital effect. However, he also found that "altered" rugose corals had $\delta^{18}O$ and $\delta^{13}C$ values very similar to that of co-occurring brachiopods and molluscs,which he ascribed to rapid cementation in the marine or shallow sediment system. It is also noteworthy that the Pennsylvanian rugose corals examined by Brand may originally have been composed of high-magnesium calcite or even aragonite (*S66*), whereas those of Devonian and younger age were composed originally of intermediate or low-magnesium calcite (*S67, S68*).

Regardless, we see no evidence of a consistent difference in $\delta^{18}O$ or Δ_{47} between rugose corals and co-occurring taxa (Fig. 3), and the vital effect observed in Kendrick Fauna rugose corals operates in the wrong direction to explain the Hirnantian excursion -also seen in brachiopods from contemporaneous sections- in our time series. Although it would be ideal to construct a curve from a single taxonomic group, this is extremely challenging for the preserved Hirnantian rock record of North America. We therefore focused our sampling on rugose corals for this unit and then made an effort to examine rugose corals in as many other units as possible. To illustrate that this is a robust strategy, we can define the entire Hirnantian excursion using only rugose corals (Fig. S10). This provides powerful evidence that the excursion is not an artifact of alteration or of taxonomic heterogeneity. Even if there were a vital effect in Late Ordovician-Early Silurian rugose corals, it could note account for the relative changes in temperature and in $\delta^{18}O_{water}$ that we observe through this interval.

K. Comparison with Cenozoic proxy data and with climate model simulations

Figure S13a plots $\delta^{18}O_{water}$ versus tropical SST, using the lowest-temperature sample from each interval as the best (e.g. least-altered) estimate as in figure 3. The nonlinearity of this relationship is striking, implying that the initial growth of Gondwanan ice sheets had little effect on tropical ocean temperatures and that following the Hirnantian maximum temperatures returned to the pre-Hirnanian range despite the persistence of moderate ice sheets. The context for evaluating this observation can be drawn by comparing the time series data with Cenozoic climate proxy records and climate model simulations of the response to increasing atmospheric CO_2 concentrations.

In panel b, there is no evidence for a nonlinear relationship between mean inferred bottom water $\delta^{18}O$ and mean tropical SST (determined by Mg/Ca paleothermometry on planktonic foraminifera), examined during several intervals in the Miocene-recent (*S69, S70*) and the Late Eocene (*S71, S72*). These data capture an interval of more than 35 Ma, and span the full range of Cenozoic glacial states from ice-free or nearly so (Late Eocene) to full bipolar glaciation (late Pleistocene) (Fig. S13b).

Simulations of state-of-the- art coupled atmosphere-ocean climate models carried out in association with the Intergovernmental Panel on Climate Change Fourth Assessment Report (*S73*) also display a linear relationship (Fig. S13c). For each model, we examine five different climates, each constructed from a 50-year average. We average years 1900-1950 and 1950-2000 from the "Climate of the 20th Century" simulation, years 2000-2050 and 2050-2100 from the SRES A1B simulation (a 720 ppm stabilization experiment), and the first 50 years after quadrupling in the "1% $\oplus yr^{-1}$ CO_2 increase to quadrupling" simulation. The tropical average temperature is computed from the time-mean surface air temperature for each climate by taking a zonal mean, linearly interpolating from the varied model grids onto a uniform latitudinal grid with 1 degree spacing, and then taking a spatial average between 20°S and 20°N. The Northern Hemisphere and Southern Hemisphere polar averages are computed using the same method but averaging instead over 70°N to 90°N or 70°S to 90°S, respectively. We include only the 15 models which reported results from these three simulations in the WCRP CMIP3 multi-model dataset:

CCCMA CGCM3.1 T47 (Canada), CNRM CM3 (France), GFDL CM2.0 (USA), GFDL CM2.1 (USA), GISS ER (USA), INGV SXG (Italy), INM CM3.0 (Russia), IPSL CM4 (France), MIROC3.2 medres (Japan), MIUB ECHO-G (Germany/Korea), MPI ECHAM5 (Germany), MRI CGCM2.3.2 (Japan), NCAR CCSM3.0 (USA), NCAR PCM1 (USA), UKMO HadGEM1 (UK). When multiple ensemble members are available from a model, we consider only the first member. Note that the CO_2 quadrupling simulations are initialized from either pre-industrial or present-day conditions, depending on the model. This difference is expected to account for some of the inter-model differences in temperature at the time of quadrupling. We acknowledge the modeling groups, the Program for Climate Model Diagnosis and Intercomparison (PCMDI), and the WCRP's Working Group on Coupled Modelling (WGCM) for their roles in making the WCRP CMIP3 multi-model dataset available for further study. Support of this dataset is provided by the Office of Science, U.S. Department of Energy. We consider "ice-free" conditions as those with annual-mean polar-average surface air temperature warmer than 0°C. To approximate last glacial maximum ("LGM" in Fig. S12b) polar temperatures, we apply previously-published results from five different coupled atmosphere-ocean climate model simulations of the difference between LGM and pre-industrial climates (*S74*). For the Northern Hemisphere, we add the inter-model mean results for central Greenland annual mean temperature change from their study (their Fig 4a) to the inter-model mean in our analysis for the temporal mean over years 1900-1950. For the Southern Hemisphere, we apply the same procedure to the central Antarctica results that they report (their Fig 4b).

From this analysis, several notable differences between our data and the Cenozoic proxy reconstructions and model simulations are clear. The pole-to-equator temperature gradient implied by the clumped isotope proxy reconstruction is larger than any of the model simulations, even under 4X CO_2 simulations. This implies that, except for perhaps the Hirnantian interval, Late Ordovician-early Silurian climate was not as efficient at transporting heat from the equator to the poles. Additionally, there is a contrast between the apparently nonlinear relationship suggested by the Ordovician-Silurian proxy time series and the linear relationship between tropical and polar temperatures in the models and quasi-linear relationship, between tropical SST and bottom water $\delta^{18}O$ in the Cenozoic proxy data (highlighted by thick shaded lines in all three panels of Fig. S13). We hypothesize that this dissemblance arises primarily from the differences between modern and Ordovician landmass distributions and associated ocean circulations. Ultimately, these differences provide support for the notion that Late Ordovician-early Silurian climate operated in a distinct fashion from that of the Late Eocene to Today.

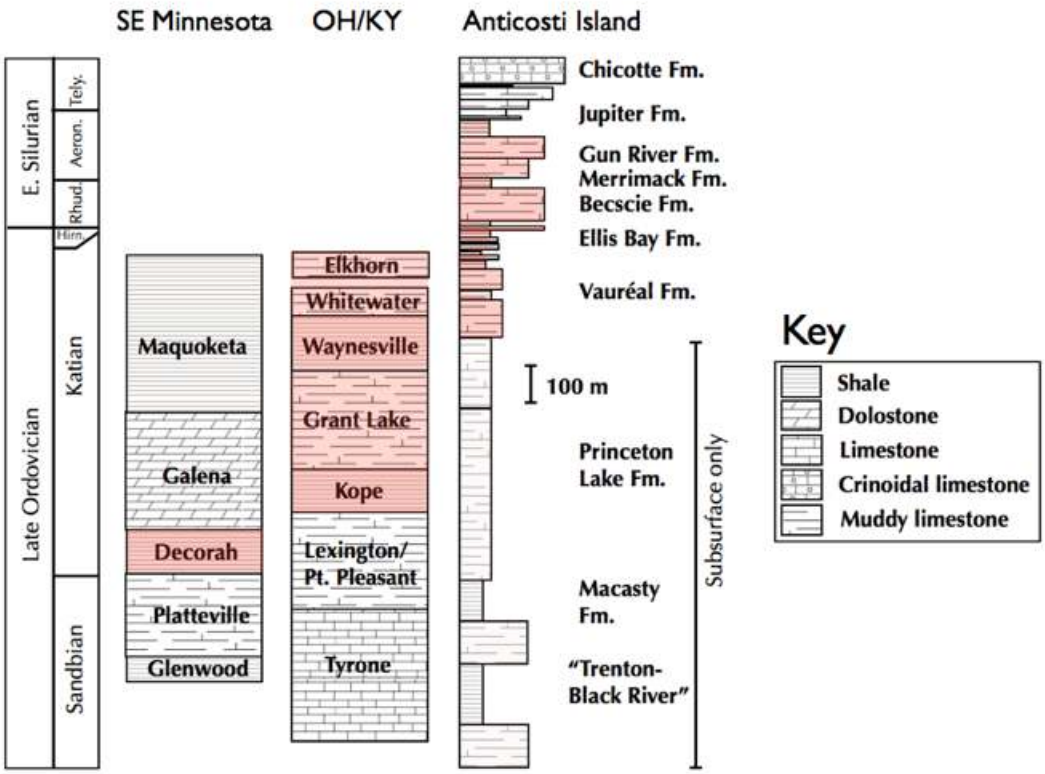

Figure S1: Lithostratographic units, shaded in red, that were sampled for this study or by Came et al., 2007 (*S38*) (Anticosti Basin column modified after Long, 2007 (*S17*). An alternative interpretation of available biostratigraphic data would place all of the Ellis Bay Formation, rather than just the Laframboise Member, in the terminal Ordovician Hirnantian Stage. Hirn. = Hirnantian, Rhud. = Rhuddanian, Aeron. = Aeronian, Tely. = Telychian.

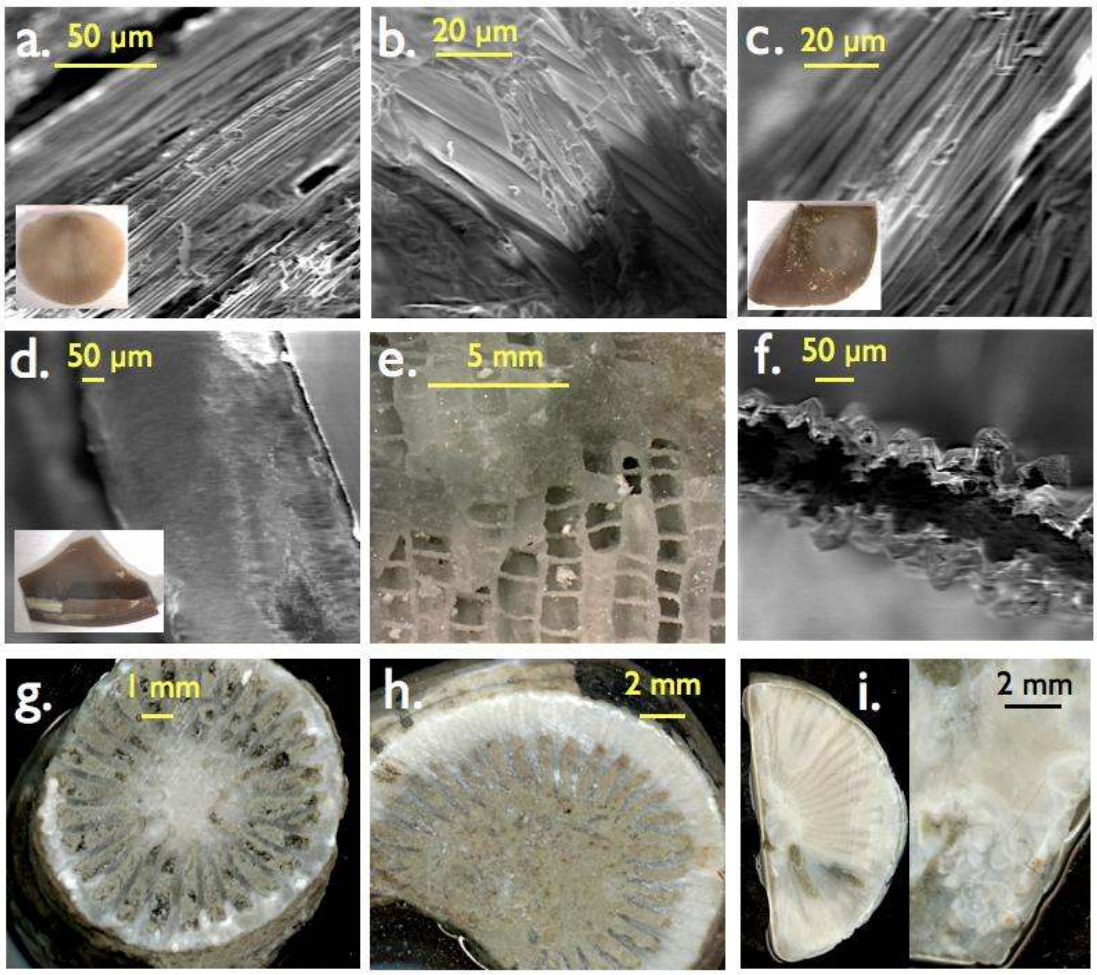

Figure S2: SEM, light microscope, and polished slab images of representative samples. a,b) brachiopod sample 912-0.8-B from the lowermost Becscie Formation, Macaire Creek, Anticosti, showing good preservation of inner prismatic layer. c) brachiopod sample Dec_B from the Decorah Formation, MN. d) trilobite sample Dec-2-T from the Decorah Formation. e) tabulate coral sample 902-0.8-TC from the upper Vauréal Formation at English Head, Anticosti Island, showing zones of both open and spar-filled corallites. f) SEM image of 902-0.8-TC showing growth of secondary calcite within open corallites, g) Tranverse section through rugose coral sample 901-12-RC2 from the Laframboise Member of the Ellis Bay Formation at Point Laframboise, Anticosti Island, showing both well-preserved and altered (white spots) areas of skeletal material and carbonate mud filling interseptal areas. g) Tranverse section through rugose coral sample 916-MF-RC2 from the Merrimack Formation along the Jupiter River, Anticosti Island. i) Transverse and longitudinal sections through rugose coral sample SGH-Lf-RC1 (not analyzed) showing extensive alteration along multiple diagenetic fronts.

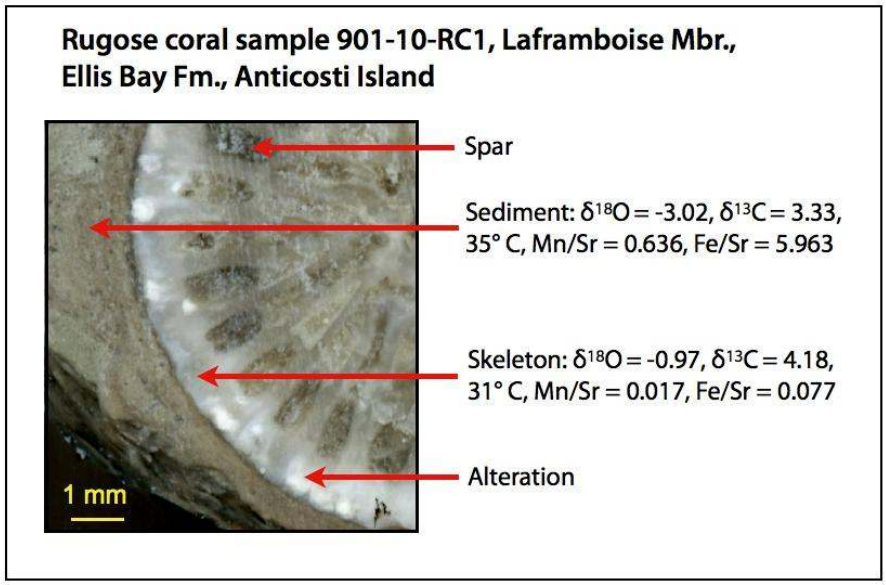

Figure S3: Transverse section through rugose coral sample 901-10-RC1, showing different phases and contrasting isotope values, clumped isotope temperatures, and trace metal concentrations from well-preserved skeletal material and from the enclosing sediment.

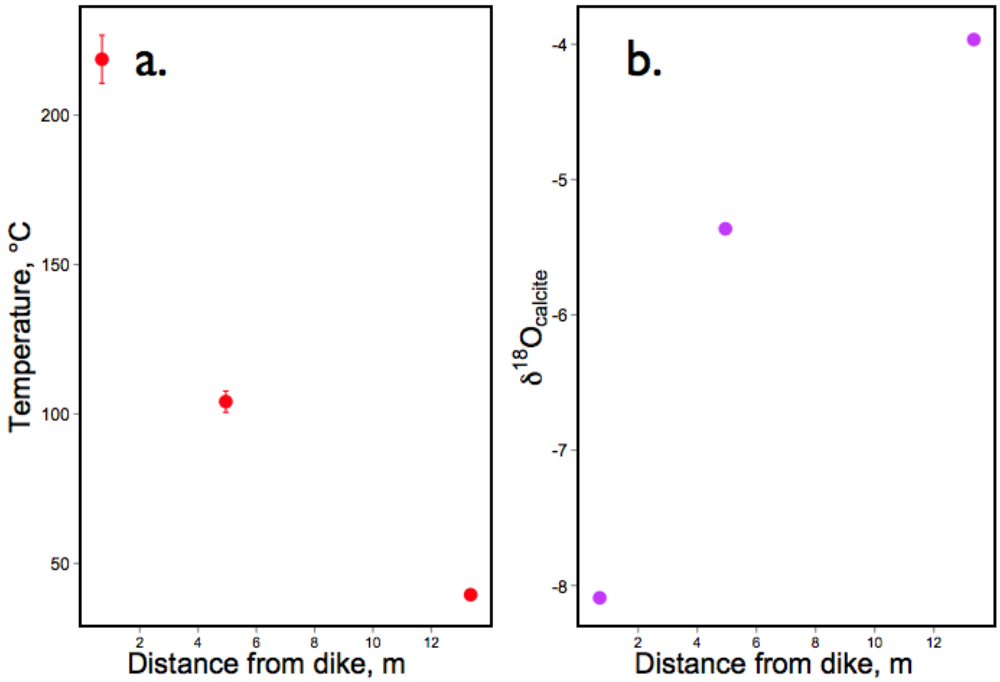

Figure S4: a) Δ_{47}-determined crystallization temperatures and b) $\delta^{18}O$ values for micritic samples from a single bed of the Vauréal Formation taken at different distances from the contact with an 8 meter thick Jurassic dike at Falaise de Puyjalons, Anticosti Island.

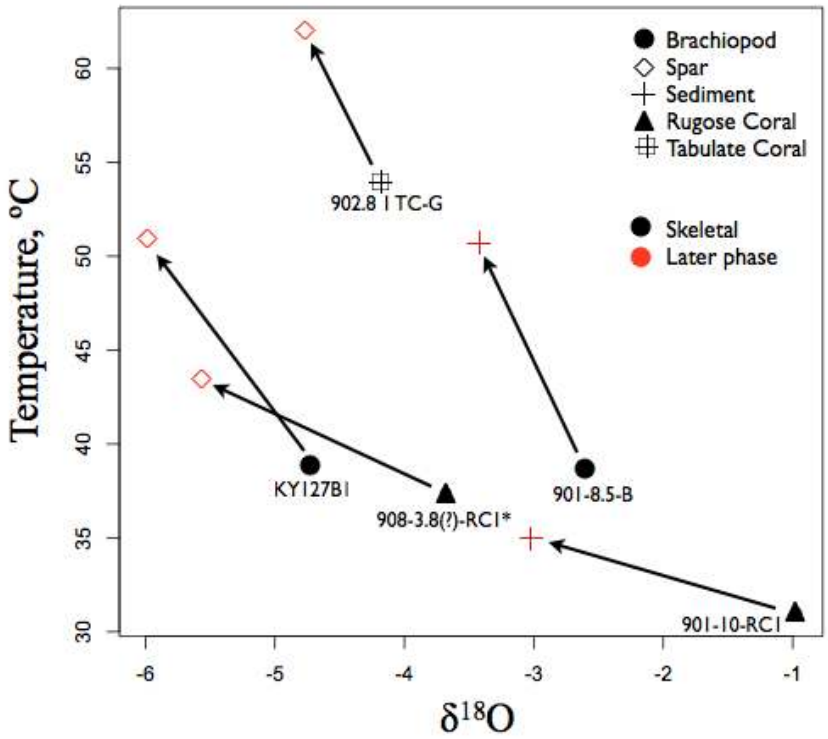

Figure S5: Crystallization temperature and $\delta^{18}O$ comparisons between skeletal phases and co-occurring phases representing later stages of carbonate precipitation (enclosing sediment or void-filling spar). Arrows connect skeletal phases to co-occurring secondary phases.*sample 908-3.8(?)-RC1 is not included in other figures and analyses due to difficulty in constraining its stratigraphic context.

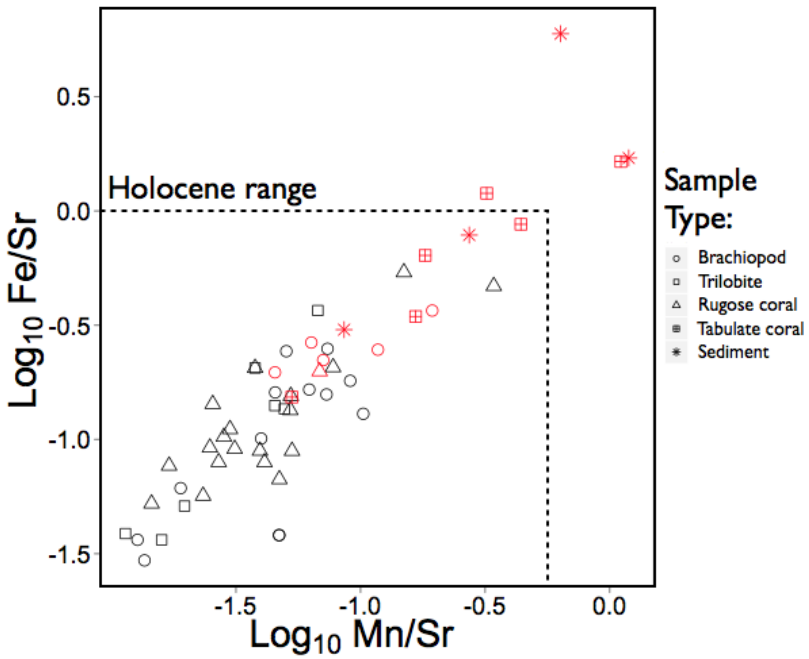

Figure S6: Mn/Sr vs. Fe/Sr for all 54 samples for which we measured trace metal concentrations. Samples indicated in red have textural evidence of alteration or are samples of sediment rather than skeletal carbonate.

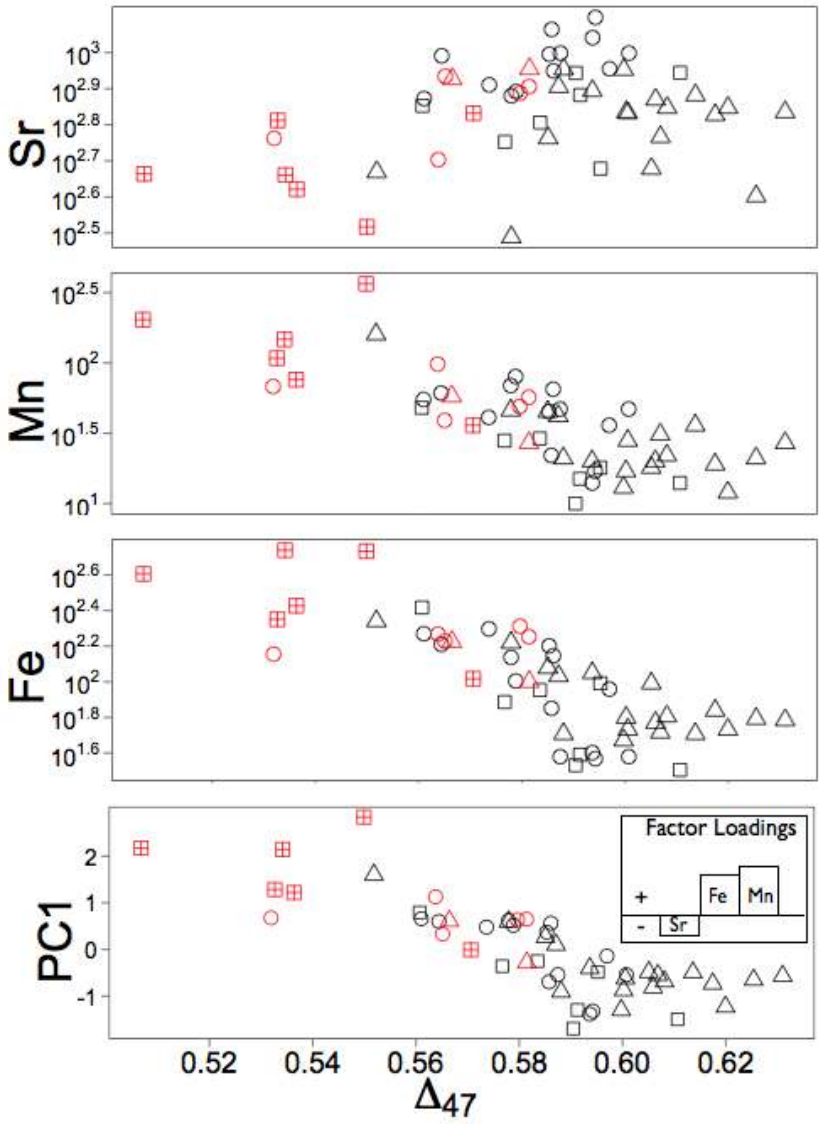

Figure S7 Trace element concentration (in ppm) plotted against Δ_{47} for Sr, Mn, and Fe, (panels 1-3) and the first principal component (PC1) of log-transformed Sr, Mn, and Fe concentration (panel 4) for all 51 skeletal carbonate samples for which trace metal concentrations were measured. Inset in panel for shows relative factor loadings for PC1, which accounts 86% of variance in trace metal concentrations. Symbols as in main text figure 2; red symbols are those with clear textural alteration.

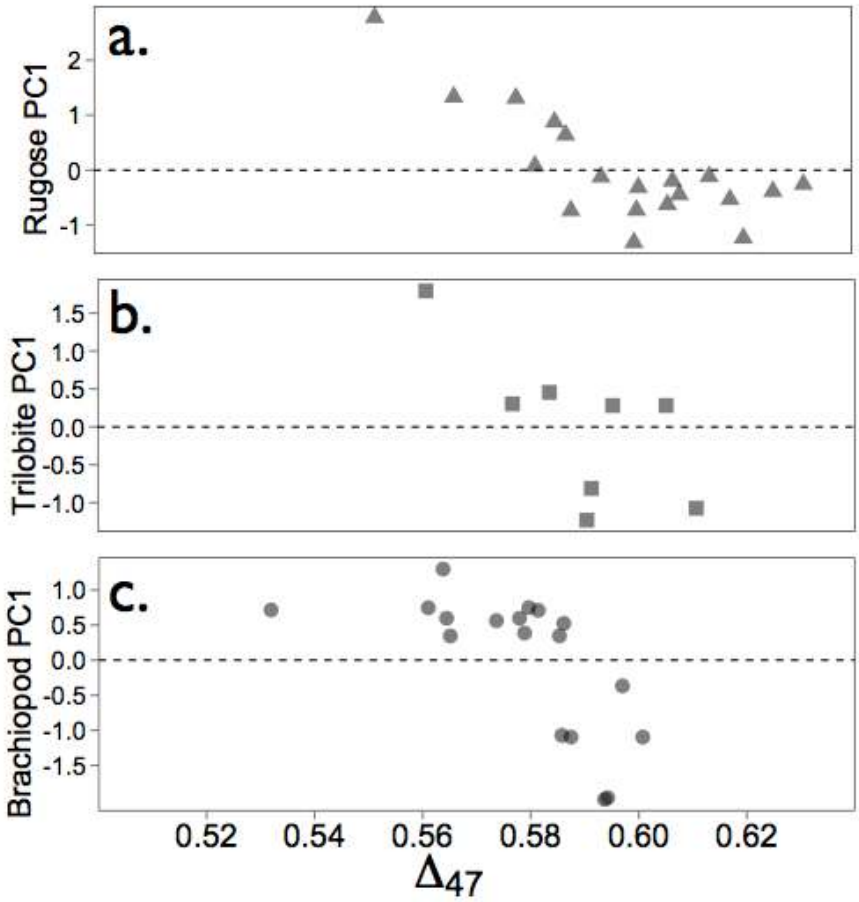

Fig. S8: The first principal component of trace metal composition plotted against Δ_{47} from taxon-specific PCA analyses of (a) rugose corals (b), trilobites, and (c) brachiopods.

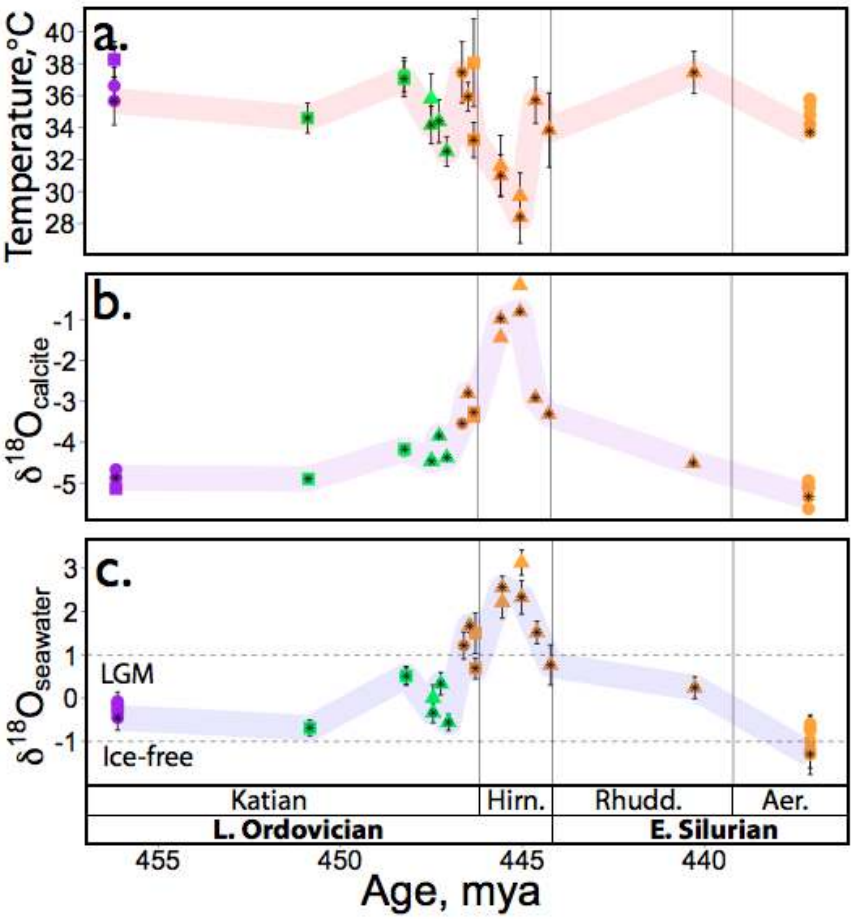

Figure S9: Reconstructed trends in (a) SST, (b) $\delta^{18}O$, and (c) $\delta^{18}O_{water}$ based only on the samples that were assayed for trace metal concentration and which have fall within the "unaltered" trace metal composition PC1 and Δ_{47} range indicated on figure 2b. Symbols, colors, error bars, and abbreviations as in main text figure 3.

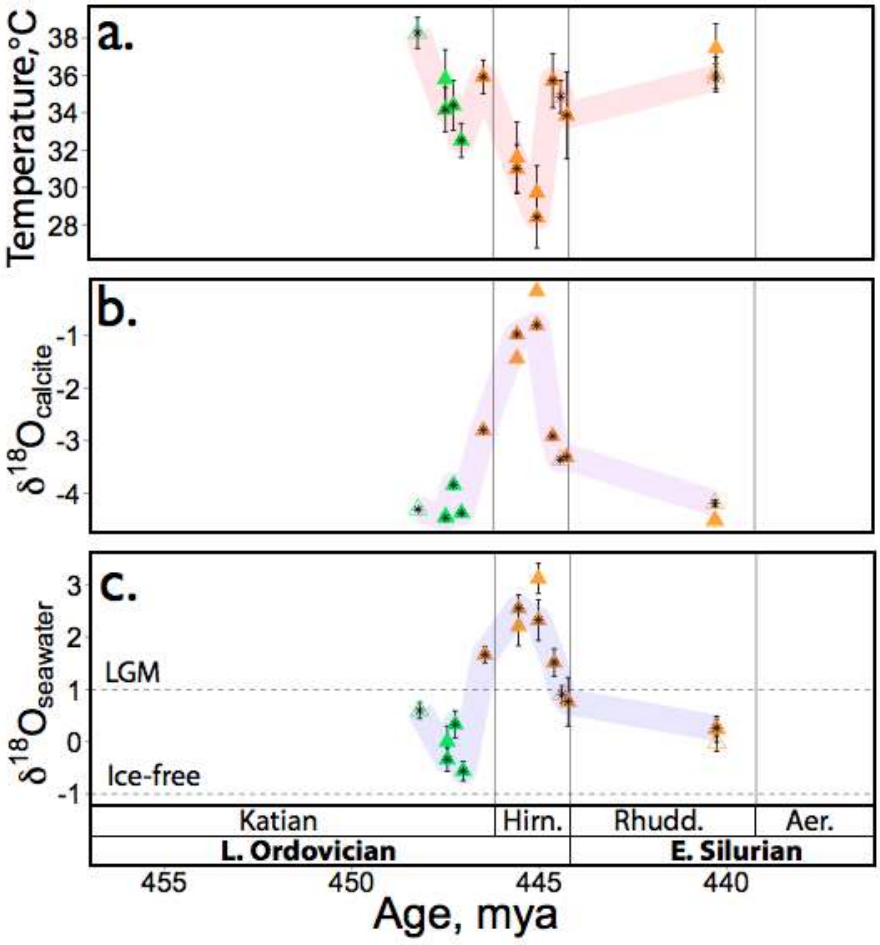

Figure S10: Trends in (a) SST, (b) $\delta^{18}O$, and (c) $\delta^{18}O_{water}$ based only on the rugose coral subset of the data presented in main text figure 3. Symbols, colors, error bars, and abbreviations as in main text figure 3.

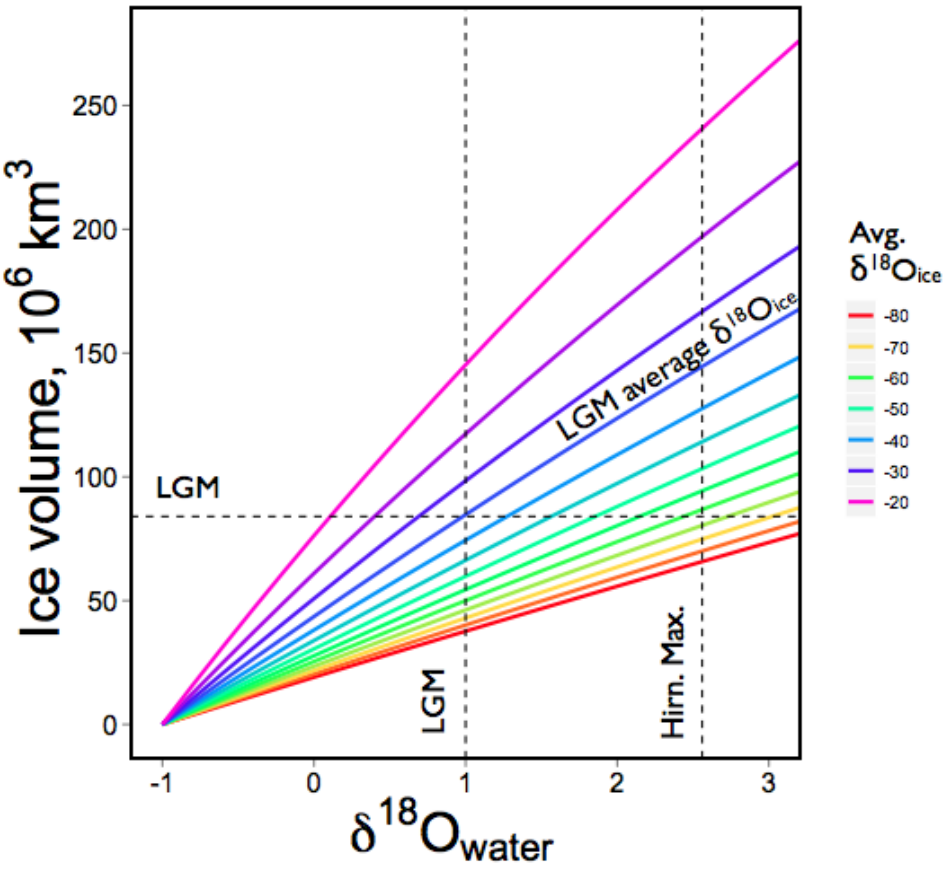

Figure S11: Inferred ice volumes (x-axis) for different measured $\delta^{18}O_{water}$ values (y-axis) using different assumptions for the mean oxygen isotopic composition of Late Ordovician-Early Silurian glacial ice (lines). Horizontal dashed line indicates inferred ice volumes for the LGM (*S27*), vertical dashed lines indicate inferred Hirnantian $\delta^{18}O_{water}$ value from this study and LGM $\delta^{18}O_{water}$ (*S45*). Average $\delta^{18}O_{ice}$ for the LGM (~-35‰) is a weighted average assuming a value of -30‰ for the now-vanished Laurentide ice sheet(*S44*) and values of -30‰ and -45‰, respectively, for remaining ice sheets in Greenland and Antarctica.

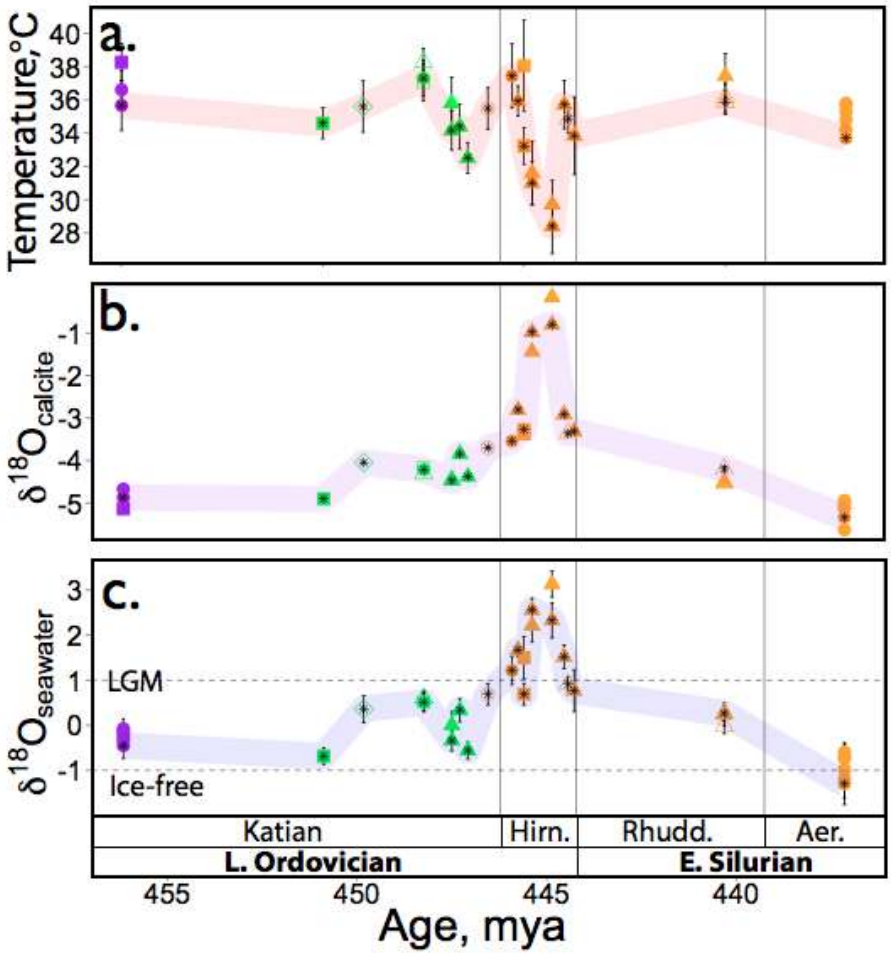

Figure S12: Trends in (a) SST, (b) $\delta^{18}O$, and (c) $\delta^{18}O_{water}$ if the sub-Laframboise members of the Ellis Bay Formation are assumed to be of early Hirnantian (rather than latest Katian) age . Symbols, colors, error bars, and abbreviations as in main text figure 3.

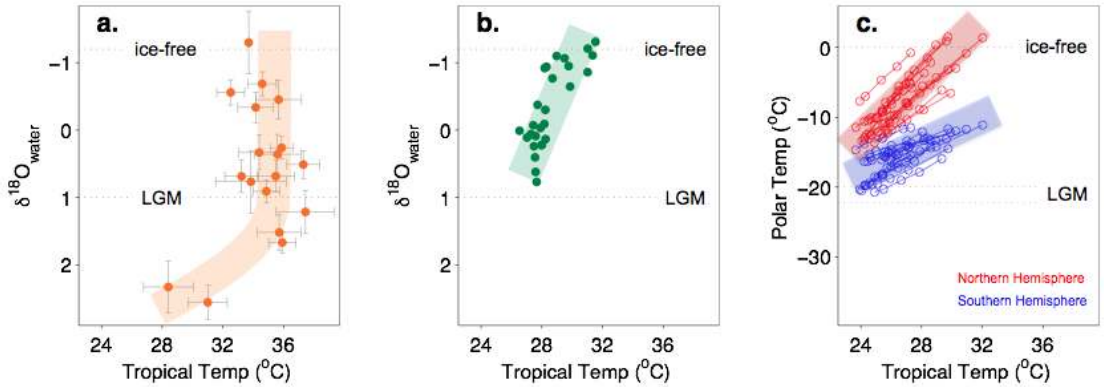

Figure S13: Comparison of Late Ordovician-early Silurian proxy reconstruction with state-of-the-art climate model simulations of modern and future conditions. a) Relationship between tropical temperature and $\delta^{18}O_{water}$ (a proxy of glacial ice volume). Values are the same as those plotted in Fig 3, except that Hirnantian and some Late Katian samples are combined into composite samples. Error bars represent the standard deviation of all observations at points with more than one measurement; at points with only one measurement they represent the analytical error on that measurement. b) Tropical SST, determined from Mg/Ca thermometry on planktonic foraminifera, vs. bottom-water $\delta^{18}O$ for several intervals in the Miocene-recent (*S69, S70*) and the Late Eocene (*S71, S72*) that span the full range of Cenozoic glacial states from ice-free or nearly so (Late Eocene) to full bipolar glaciation (late Pleistocene). Points represent averages within 0.2 myr time bins. c) Results from coupled atmosphere-ocean climate model simulations of climates varying from early 20th century to quadrupled CO_2 (see SOM "Comparison with climate model simulations" section). Each point represents a different simulated climate plotted in terms of tropical temperature versus Northern Hemisphere (red) or Southern Hemisphere (blue) polar temperature. Each line connects runs of the same model under different CO_2 forcing. The inter-model mean slope of the lines is 0.49 [1 / 2.058(1.4-3.1)] for the Northern Hemisphere and 1.0 [1 / 0.996(0.6-2.1)] for the Southern Hemisphere, consistent with previous analyses of Northern Hemisphere polar amplification (*S75*). Note that the analogy made here between the proxy reconstruction and model simulations assumes that the relationship between ice volume and polar temperature can be approximated as linear within the range plotted here.

Table S1: Source, type, locality, stratigraphic context, estimated age, δ13C, δ18O, Δ47, temperature, δ18Owater, textural alteration status, and trace metal data for samples referred to in text and SOM.

sample	source	taxon	formation	member	stage	age, Ma
A1391b-31	Came et al., 2007	Brachiopod	Jupiter Fm.		L. Aeronian	437
A1391b-31	Came et al., 2007	Brachiopod	Jupiter Fm.		L. Aeronian	437
A1391b-06	Came et al., 2007	Brachiopod	Jupiter Fm.		L. Aeronian	437
A1391b-06	Came et al., 2007	Brachiopod	Jupiter Fm.		L. Aeronian	437
A1380b-30	Came et al., 2007	Brachiopod	Jupiter Fm.		L. Aeronian	437
A1356a-37	Came et al., 2007	Brachiopod	Jupiter Fm.		L. Aeronian	437
A1356a-07	Came et al., 2007	Brachiopod	Jupiter Fm.		L. Aeronian	437
A1356a-07	Came et al., 2007	Brachiopod	Jupiter Fm.		L. Aeronian	437
A-958-4 alt	Came et al., 2007	Brachiopod	Jupiter Fm.		L. Aeronian	437
A-958-3	Came et al., 2007	Brachiopod	Jupiter Fm.		L. Aeronian	437
A-958-2 alt	Came et al., 2007	Brachiopod	Jupiter Fm.		L. Aeronian	437
A-958	Came et al., 2007	Brachiopod	Jupiter Fm.		L. Aeronian	437
A 551 alt	Came et al., 2007	Brachiopod	Jupiter Fm.		L. Aeronian	437
922-F-RC	this study	Rugose coral	Gun River Fm.	Macgilvray	L. Aeronian	438
922 2 TC G	this study	Tabulate coral	Gun River Fm.	Macgilvray	L. Aeronian	438
922 1 TC S	this study	Tabulate coral	Gun River Fm.	Macgilvray	L. Aeronian	438
923-0.9-RC	this study	Rugose coral	Becscie Fm.	Chabot	L. Rhuddanian	440
916MF 3 RC	this study	Rugose coral	Merrimack Fm.	-	L. Rhuddanian	440
916MF 2 B	this study	Brachiopod	Merrimack Fm.	-	L. Rhuddanian	440
916 RC 2	this study	Rugose coral	Becscie Fm.	Chabot	L. Rhuddanian	440
916 MF RC2	this study	Rugose coral	Merrimack Fm.	-	L. Rhuddanian	440
916 MF B 4	this study	Brachiopod	Merrimack Fm.	-	L. Rhuddanian	440
916 MF 1 B	this study	Brachiopod	Merrimack Fm.	-	L. Rhuddanian	440
916 Bc RC	this study	Rugose coral	Becscie Fm.	Chabot	L. Rhuddanian	440
916 B SI	this study	Brachiopod	Merrimack Fm.	-	L. Rhuddanian	440
901 19 RC 2	this study	Rugose coral	Becscie Fm.	Fox Point	L. Hirnantian	443.5
Lbec F B	this study	Brachiopod	Becscie Fm.	Fox Point	L. Hirnantian	443.5
912.98 2 RC	this study	Rugose coral	Becscie Fm.	Fox Point	L. Hirnantian	443.5
912 .98 1B	this study	Brachiopod	Becscie Fm.	Fox Point	L. Hirnantian	443.5
911 2.1 RC	this study	Rugose coral	Becscie Fm.	Fox Point	L. Hirnantian	443.5
912.98 B2	this study	Brachiopod	Becscie Fm.	Fox Point	L. Hirnantian	443.5
901-15-RC1	this study	Rugose coral	Becscie Fm.	Fox Point	Hirnantian	443.5
901-12-RC3	this study	Rugose coral	Ellis Bay Fm.	Laframboise	Hirnantian	444.5
901-12-RC2	this study	Rugose coral	Ellis Bay Fm.	Laframboise	Hirnantian	444.5
901 12 TC	this study	Tabulate coral	Ellis Bay Fm.	Laframboise	Hirnantian	444.5
901 12 RC 1	this study	Rugose coral	Ellis Bay Fm.	Laframboise	Hirnantian	444.5
901 12 LRC	this study	Rugose coral	Ellis Bay Fm.	Laframboise	Hirnantian	444.5
901.11 1 TC	this study	Tabulate coral	Ellis Bay Fm.	Laframboise	Hirnantian	444.75
901 10 RC 2	this study	Rugose coral	Ellis Bay Fm.	Laframboise	Hirnantian	445
901 10 RC 1	this study	Rugose coral	Ellis Bay Fm.	Laframboise	Hirnantian	445
901 8.5 B	this study	Brachiopod	Ellis Bay Fm.	Laframboise	Hirnantian	445.5
912.8 B 2	this study	Brachiopod	Ellis Bay Fm.	Lousy Cove	L. Katian	445.7
912-.8 2 T	this study	Trilobite	Ellis Bay Fm.	Lousy Cove	L. Katian	445.7
912 0.8 B	this study	Brachiopod	Ellis Bay Fm.	Lousy Cove	L. Katian	445.7
908 1 T	this study	Trilobite	Ellis Bay Fm.	Lousy Cove	L. Katian	445.7
904.4 2 RC	this study	Rugose coral	Ellis Bay Fm.	Prinsta	L. Katian	446
904.25 1 B	this study	Brachiopod	Ellis Bay Fm.	Prinsta	L. Katian	446
904 4.5 RC	this study	Rugose coral	Ellis Bay Fm.	Prinsta	L. Katian	446

Table S1: Source, type, locality, stratigraphic context, estimated age, δ13C, δ18O, Δ47, temperature, δ18Owater, textural alteration status, and trace metal data for samples referred to in text and SOM.

sample	source	taxon	formation	member	stage	age, Ma
904 .4 B1	this study	Brachiopod	Ellis Bay Fm.	Prinsta	L. Katian	446
904 .4 1RC	this study	Rugose coral	Ellis Bay Fm.	Prinsta	L. Katian	446
ElkR1	this study	Rugose coral	Elkhorn Fm.	-	L. Katian	446.5
ElkR2	this study	Rugose coral	Elkhorn Fm.	-	L. Katian	446.7
WWR1	this study	Rugose coral	Whitewater Fm.	-	L. Katian	446.8
WWR2	this study	Rugose coral	Whitewater Fm.	-	L. Katian	446.8
Wayne Bb	this study	Brachiopod	Waynesville Fm.	Blanchester	L. Katian	447
918-52 1 B	this study	Brachiopod	Vaureal Fm.	Joseph Point?	L. Katian	447
918-43.2 1 B	this study	Brachiopod	Vaureal Fm.	Joseph Point?	L. Katian	447
918 52 B2	this study	Brachiopod	Vaureal Fm.	Joseph Point?	L. Katian	447
918 43.2 B2a	this study	Brachiopod	Vaureal Fm.	Joseph Point?	L. Katian	447
918 43.2 B	this study	Brachiopod	Vaureal Fm.	Joseph Point?	L. Katian	447
918 43.2	this study	Brachiopod	Vaureal Fm.	Joseph Point?	L. Katian	447
907.23F 1 B	this study	Brachiopod	Vaureal Fm.	Lavache	L. Katian	447
906 23-30 T1	this study	Trilobite	Vaureal Fm.	Lavache	L. Katian	447
906 23-30 1 B	this study	Brachiopod	Vaureal Fm.	Lavache	L. Katian	447
906 2 T	this study	Trilobite	Vaureal Fm.	Lavache	L. Katian	447
906 1 T	this study	Trilobite	Vaureal Fm.	Lavache	L. Katian	447
902.8 2 TC-S	this study	Tabulate coral	Vaureal Fm.	"English Head"	L. Katian	447
902.8 1 TC-G	this study	Tabulate coral	Vaureal Fm.	"English Head"	L. Katian	447
SGH-W 43.0 T1	this study	Trilobite	Waynesville Fm.	Blanchester	L. Katian	447
SGH-W-43.0 Cr1	this study	Crinoid	Waynesville Fm.	Blanchester	L. Katian	447
SGH-W-43.0-B1	this study	Brachiopod	Waynesville Fm.	Blanchester	L. Katian	447
SGH-W-42.2 R1	this study	Rugose coral	Waynesville Fm.	Blanchester	L. Katian	447
KY127B1	this study	Brachiopod	Grant Lake Fm.	Bellevue	L. Katian	448
KY127Bry1	this study	Bryozoan	Grant Lake Fm.	Bellevue	L. Katian	448
MCc-F-4.8-Bry1	this study	Bryozoan	Fairview Fm.	Mount Hope	L. Katian	448
Mol Isotelus b	this study	Trilobite	Kope Fm.	McMicken	M. Katian	449
MM1-Bb	this study	Brachiopod	Kope Fm.	McMicken	M. Katian	449
HC-K T1	this study	Trilobite	Kope Fm.	Economy	M. Katian	449
HC-K-18-B1	this study	Brachiopod	Kope Fm.	Economy	M. Katian	449
Dec B1	this study	Brachiopod	Decorah Fm.	Spechts Ferry	E. Katian	455
Dec B2	this study	Brachiopod	Decorah Fm.	Spechts Ferry	E. Katian	455
Dec T1	this study	Trilobite	Decorah Fm.	Spechts Ferry	E. Katian	455

Table S1: Source, type, locality, stratigraphic context, estimated age, δ13C, δ18O, Δ47, temperature, δ18Owater, textural alteration status, and trace metal data for samples referred to in text and SOM.

sample	locality	type	sample	latitude	longitude
A1391b-31	A-1391 (see P. Copper locality register)	Supplied by J. Veizer	A1391b-31	-	-
A1391b-31	A-1391 (see P. Copper locality register)	Supplied by J. Veizer	A1391b-31	-	-
A1391b-06	A-1391 (see P. Copper locality register)	Supplied by J. Veizer	A1391b-06	-	-
A1391b-06	A-1391 (see P. Copper locality register)	Supplied by J. Veizer	A1391b-06	-	-
A1380b-30	A-1380 (see P. Copper locality register)	Supplied by J. Veizer	A1380b-30	-	-
A1356a-37	A-1356 (see P. Copper locality register)	Supplied by J. Veizer	A1356a-37	-	-
A1356a-07	A-1356 (see P. Copper locality register)	Supplied by J. Veizer	A1356a-07	-	-
A1356a-07	A-1356 (see P. Copper locality register)	Supplied by J. Veizer	A1356a-07	-	-
A-958-4 alt	A-958 (see P. Copper locality register)	Supplied by J. Veizer	A-958-4 alt	-	-
A-958-3	A-958 (see P. Copper locality register)	Supplied by J. Veizer	A-958-3	-	-
A-958-2 alt	A-958 (see P. Copper locality register)	Supplied by J. Veizer	A-958-2 alt	-	-
A-958	A-958 (see P. Copper locality register)	Supplied by J. Veizer	A-958	-	-
A 551 alt	A-551 (see P. Copper locality register)	Supplied by J. Veizer	A 551 alt	-	-
922-F-RC	E. of Mouth of Riviere la Loutre, Anticosti	Field collection	922-F-RC	N 49° 36.374'	W 63° 47.175'
922 2 TC G	E. of Mouth of Riviere la Loutre, Anticosti	Field collection	922 2 TC G	N 49° 36.374'	W 63° 47.175'
922 1 TC S	E. of Mouth of Riviere la Loutre, Anticosti	Field collection	922 1 TC S	N 49° 36.374'	W 63° 47.175'
923-0.9-RC	Mouth of Riviere aux Cailloux, Anticosti	Field collection	923-0.9-RC	N 49° 38.969'	W 63° 52.063'
916MF 3 RC	Riviere Jupiter, Anticosti,	Field collection	916MF 3 RC	N 49° 36.799'	W 63° 26.548'
916MF 2 B	Riviere Jupiter, Anticosti	Field collection	916MF 2 B	N 49° 36.799'	W 63° 26.548'
916 RC 2	Riviere Jupiter, Anticosti	Field collection	916 RC 2	N 49° 36.799'	W 63° 26.548'
916 MF RC2	Riviere Jupiter, Anticosti	Field collection	916 MF RC2	N 49° 36.799'	W 63° 26.548'
916 MF B 4	Riviere Jupiter, Anticosti	Field collection	916 MF B 4	N 49° 36.799'	W 63° 26.548'
916 MF 1 B	Riviere Jupiter, Anticosti	Field collection	916 MF 1 B	N 49° 36.799'	W 63° 26.548'
916 Bc RC	Riviere Jupiter, Anticosti	Field collection	916 Bc RC	N 49° 36.799'	W 63° 26.548'
916 B SI	Riviere Jupiter, Anticosti	Field collection	916 B SI	N 49° 36.799'	W 63° 26.548'
901 19 RC 2	Point Laframboise, Anticosti	Field collection	901 19 RC 2	N 49° 48.350'	W 64° 25.259'
Lbec F B	Riviere aux Saumon, Anticosti	Field collection	Lbec F B	N 49° 24.015'	W 62° 23.175'
912.98 2 RC	MacCaire Creek, Anticosti	Field collection	912.98 2 RC	N 49° 22.762'	W 62° 12.320'
912 .98 1B	MacCaire Creek, Anticosti	Field collection	912 .98 1B	N 49° 22.762'	W 62° 12.320'
911 2.1 RC	Riviere aux Saumon, Anticosti	Field collection	911 2.1 RC	N 49° 23.853'	W 62° 23.583'
912.98 B2	MacCaire Creek, Anticosti	Field collection	912.98 B2	N 49° 22.762'	W 62° 12.320'
901-15-RC1	Point Laframboise, Anticosti	Field collection	901-12-RC3	N 49° 48.350'	W 64° 25.259'
901-12-RC3	Point Laframboise, Anticosti	Field collection	901-12-RC3	N 49° 48.350'	W 64° 25.259'
901-12-RC2	Point Laframboise, Anticosti	Field collection	901-12-RC2	N 49° 48.350'	W 64° 25.259'
901 12 TC	Point Laframboise, Anticosti	Field collection	901 12 TC	N 49° 48.350'	W 64° 25.259'
901 12 RC 1	Point Laframboise, Anticosti	Field collection	901 12 RC 1	N 49° 48.350'	W 64° 25.259'
901 12 LRC	Point Laframboise, Anticosti	Field collection	901 12 LRC	N 49° 48.350'	W 64° 25.259'
901.11 1 TC	Point Laframboise, Anticosti	Field collection	901.11 1 TC	N 49° 48.350'	W 64° 25.259'
901 10 RC 2	Point Laframboise, Anticosti	Field collection	901 10 RC 2	N 49° 48.350'	W 64° 25.259'
901 10 RC 1	Point Laframboise, Anticosti	Field collection	901 10 RC 1	N 49° 48.350'	W 64° 25.259'
901 8.5 B	Point Laframboise, Anticosti	Field collection	901 8.5 B	N 49° 48.350'	W 64° 25.259'
912.8 B 2	MacCaire Creek, Anticosti	Field collection	912.8 B 2	N 49° 22.762'	W 62° 12.320'
912-.8 2 T	MacCaire Creek, Anticosti	Field collection	912-.8 2 T	N 49° 22.762'	W 62° 12.320'
912 0.8 B	MacCaire Creek, Anticosti	Field collection	912 0.8 B	N 49° 22.762'	W 62° 12.320'
908 1 T	Riviere aux Saumon, Anticosti	Field collection	908 1 T	N 49° 24.015'	W 62° 23.175'
904.4 2 RC	Between Junction Cliff and Pt. Laframboise, Anticosti	Field collection	904.4 2 RC	N 49° 49.567'	W 64° 26.574'
904.25 1 B	Between Junction Cliff and Pt. Laframboise, Anticosti	Field collection	904.25 1 B	N 49° 49.567'	W 64° 26.574'
904 4.5 RC	Between Junction Cliff and Pt. Laframboise, Anticosti	Field collection	904 4.5 RC	N 49° 49.567'	W 64° 26.574'

Table S1: Source, type, locality, stratigraphic context, estimated age, δ13C, δ18O, Δ47, temperature, δ18Owater, textural alteration status, and trace metal data for samples referred to in text and SOM.

sample	locality	type	sample	latitude	longitude
904 .4 B1	Between Junction Cliff and Pt. Laframboise, Anticosti	Field collection	904 .4 B1	N 49° 49.567'	W 64° 26.574'
904 .4 1RC	Between Junction Cliff and Pt. Laframboise, Anticosti	Field collection	904 .4 1RC	N 49° 49.567'	W 64° 26.574'
ElkR1	-	Cin. Mus. Nat. Hist. Coll.	ElkR1	-	-
ElkR2	Osgood Road & Cedar Creek, Versailles, IN	Cin. Mus. Nat. Hist. Coll.	ElkR2	N 38° 12' 18"	W 84° 19' 45"
WWR1	State Line Road and Short Creek, Richmond, IN	Cin. Mus. Nat. Hist. Coll.	WWR1	N 39°48' 35"	W 84° 48' 50"
WWR2	State Line Road and Short Creek, Richmond, IN	Cin. Mus. Nat. Hist. Coll.	WWR2	N 39°48' 35"	W 84° 48' 50"
Wayne Bb	Richmond, IN: Cinc. Mus. of Nat. Hist. Collections	Cin. Mus. Nat. Hist. Coll.	Wayne Bb	N 39°48' 35"	W 84° 48' 50"
918-52 1 B	Baie des Homards, Anticosti	Field collection	918-52 1 B	N 49° 27.889'	W 62° 18.782'
918-43.2 1 B	Baie des Homards, Anticosti	Field collection	918-43.2 1 B	N 49° 27.889'	W 62° 18.782'
918 52 B2	Baie des Homards, Anticosti	Field collection	918 52 B2	N 49° 27.889'	W 62° 18.782'
918 43.2 B2a	Baie des Homards, Anticosti	Field collection	918 43.2 B2a	N 49° 27.889'	W 62° 18.782'
918 43.2 B	Baie des Homards, Anticosti	Field collection	918 43.2 B	N 49° 27.889'	W 62° 18.782'
918 43.2	Baie des Homards, Anticosti	Field collection	918 43.2	N 49° 27.889'	W 62° 18.782'
907.23F 1 B	Riviere Kalamazoo, Anticosti	Field collection	907.23F 1 B	N 49° 46.369'	W 63° 31.663'
906 23-30 T1	Riviere L'Huile, Anticosti	Field collection	906 23-30 T1	N 49° 50.507'	W 63° 33.222'
906 23-30 1 B	Riviere L'Huile, Anticosti	Field collection	906 23-30 1 B	N 49° 50.507'	W 63° 33.222'
906 2 T	Riviere L'Huile, Anticosti	Field collection	906 2 T	N 49° 50.507'	W 63° 33.222'
906 1 T	Riviere L'Huile, Anticosti	Field collection	906 1 T	N 49° 50.507'	W 63° 33.222'
902.8 2 TC-S	English Head, Anticosti	Field collection	902.8 2 TC-S	N 49° 54.072'	W 64° 29.458'
902.8 1 TC-G	English Head, Anticosti	Field collection	902.8 1 TC-G	N 49° 54.072'	W 64° 29.458'
SGH-W 43.0 T1	South Gate Hill cut, IN Route 1, Cedar Grove, IN	Field collection	SGH-W 43.0 T1	N 39° 21' 30"	W 84° 30' 38"
SGH-W-43.0 Cr1	South Gate Hill cut, IN Route 1, Cedar Grove, IN	Field collection	SGH-W-43.0 Cr1	N 39° 21' 30"	W 84° 30' 38"
SGH-W-43.0-B1	South Gate Hill cut, IN Route 1, Cedar Grove, IN	Field collection	SGH-W-43.0-B1	N 39° 21' 30"	W 84° 30' 38"
SGH-W-42.2 R1	South Gate Hill cut, IN Route 1, Cedar Grove, IN	Field collection	SGH-W-42.2 R1	N 39° 21' 30"	W 84° 30' 38"
KY127B1	small cut 1.4 miles north of Monterey E. cut, KY 127	Field collection	KY127B1	N 38° 16' 55"	W 84° 50' 53"
KY127Bry1	small cut 1.4 miles north of Monterey E. cut, KY 127	Field collection	KY127Bry1	N 38° 16' 55"	W 84° 50' 53"
MCc-F-4.8-Bry1	Maysville, KY, cut on Hwy 62/68	Field collection	MCc-F-4.8-Bry1	N 38° 40' 46"	W 83° 47' 42"
Mol Isotelus b	Maysville, KY: Cinc. Mus. of Nat. Hist. Collections	Cin. Mus. Nat. Hist. Coll.	Mol Isotelus b	N 38° 40' 51"	W 83° 47' 34"
MM1-Bb	Maysville, KY: Cinc. Mus. of Nat. Hist. Collections	Cin. Mus. Nat. Hist. Coll.	MM1-Bb	N 38° 40' 51"	W 83° 47' 34"
HC-K T1	Holst Creek road cut on KY state route 9	Field collection	HC-K T1	N 38° 46' 33"	W 84° 12' 20"
HC-K-18-B1	Holst Creek road cut on KY state route 9	Field collection	HC-K-18-B1	N 38° 46' 33"	W 84° 12' 20"
Dec B1	Wang's Corner, MN	Field collection	Dec B + spar	-	-
Dec B2	Wang's Corner, MN	Field collection	Dec B	-	-
Dec T1	Wang's Corner, MN	Field collection	DEC 2 T	-	-

Table S1: Source, type, locality, stratigraphic context, estimated age, δ13C, δ18O, Δ47, temperature, δ18Owater, textural alteration status, and trace metal data for samples referred to in text and SOM.

sample	# analyses	δ13C (PBD)	δ13C stdev	δ18O (PBD)	δ18O stdev	Δ_{47}	Δ_{47} stdev	Temp. (° C)	temp. stdev
A1391b-31	1	2.03	-	-4.940	-	0.602	-	35.3	-
A1391b-31	1	2.08	-	-5.000	-	0.604	-	34.8	-
A1391b-06	1	1.78	-	-5.110	-	0.601	-	35.7	-
A1391b-06	1	1.71	-	-5.120	-	0.607	-	34.2	-
A1380b-30	1	1.94	-	-5.340	-	0.609	-	33.7	-
A1356a-37	1	1.82	-	-5.630	-	0.600	-	35.8	-
A1356a-07	1	1.71	-	-5.100	-	0.569	-	43.9	-
A1356a-07	1	1.73	-	-5.070	-	0.573	-	42.9	-
A-958-4 alt	1	0.21	-	-4.880	-	0.524	-	56.7	-
A-958-3	1	0.86	-	-4.880	-	0.537	-	53.0	-
A-958-2 alt	1	-0.03	-	-5.200	-	0.509	-	61.3	-
A-958	1	0.18	-	-5.120	-	0.506	-	62.4	-
A 551 alt	1	-1.13	-	-5.220	-	0.501	-	63.8	-
922-F-RC	1	1.524	0.011	-3.256	0.019	0.557	0.025	47.3	2.4
922 2 TC G	1	1.348	0.014	-5.386	0.025	0.534	0.039	53.7	4.0
922 1 TC S	1	1.188	0.017	-5.683	0.034	0.536	0.038	53.0	3.9
923-0.9-RC	1	1.355	0.010	-4.486	0.019	0.552	0.029	48.6	2.8
916MF 3 RC	3	1.883	0.008	-4.194	0.094	0.600	0.015	35.9	2.1
916MF 2 B	2	1.166	0.016	-4.478	0.020	0.586	0.021	39.4	3.7
916 RC 2	1	0.965	0.004	-4.527	0.005	0.599	0.028	36.1	2.4
916 MF RC2	1	1.042	0.019	-4.512	0.037	0.594	0.042	37.4	3.7
916 MF B 4	1	1.318	0.017	-4.328	0.032	0.587	0.034	39.0	3.0
916 MF 1 B	1	1.321	0.021	-4.059	0.041	0.574	0.034	42.6	3.2
916 Bc RC	1	1.486	0.009	-4.668	0.020	0.566	0.027	44.6	2.5
916 B SI	1	0.868	0.016	-4.954	0.035	0.578	0.032	41.5	3.0
901 19 RC 2	3	1.054	0.024	-3.312	0.039	0.608	0.018	33.8	2.5
Lbec F B	1	1.798	0.009	-3.591	0.012	0.585	0.036	39.6	3.3
912.98 2 RC	2	2.070	0.004	-3.617	0.042	0.587	0.016	39.1	2.9
912 .98 1B	4	2.115	0.016	-3.594	0.101	0.579	0.014	41.3	1.8
911 2.1 RC	3	2.162	0.033	-2.916	0.025	0.601	0.014	35.7	2.0
912.98 B2	1	2.427	0.017	-3.456	0.032	0.564	0.030	45.1	2.9
901-15-RC1	1	0.647	0.002	-3.362	0.004	0.604	0.026	34.9	2.3
901-12-RC3	1	3.694	0.005	-3.130	0.008	0.585	0.029	39.6	2.6
901-12-RC2	5	4.059	0.041	-0.803	0.108	0.631	0.016	28.4	1.6
901 12 TC	1	3.001	0.006	-4.589	0.004	0.571	0.039	43.5	3.6
901 12 RC 1	2	4.468	0.059	-0.159	0.042	0.625	0.025	29.7	4.1
901 12 LRC	1	3.113	0.013	-3.699	0.035	0.581	0.023	40.6	2.1
901.11 1 TC	1	3.443	0.019	-4.033	0.033	0.550	0.041	49.1	4.0
901 10 RC 2	4	4.834	0.035	-1.438	0.015	0.617	0.014	31.6	1.6
901 10 RC 1	2	4.184	0.003	-0.979	0.032	0.620	0.022	31.0	3.6
901 8.5 B	2	2.250	0.005	-2.603	0.014	0.589	0.021	38.5	3.7
912.8 B 2	1	0.737	0.023	-3.455	0.045	0.553	0.044	48.2	4.3
912-.8 2 T	3	0.135	0.017	-3.370	0.065	0.591	0.017	38.0	2.5
912 0.8 B	4	0.849	0.016	-3.071	0.103	0.561	0.018	46.0	2.5
908 1 T	4	0.041	0.020	-3.272	0.117	0.611	0.015	33.2	1.9
904.4 2 RC	1	2.170	0.012	-2.822	0.026	0.578	0.022	41.5	2.0
904.25 1 B	1	1.059	0.016	-4.188	0.026	0.532	0.015	54.4	1.6
904 4.5 RC	3	2.489	0.006	-2.806	0.030	0.600	0.019	35.9	2.7

Table S1: Source, type, locality, stratigraphic context, estimated age, δ13C, δ18O, Δ47, temperature, δ18Owater, textural alteration status, and trace metal data for samples referred to in text and SOM.

sample	# analyses	δ13C (PBD)	δ13C stdev	δ18O (PBD)	δ18O stdev	Δ_{47}	Δ_{47} stdev	Temp. (° C)	temp. stdev
904 .4 B1	3	1.769	0.026	-3.542	0.077	0.594	0.023	37.4	3.4
904 .4 1RC	1	0.838	0.003	-2.773	0.003	0.588	0.023	38.9	2.1
ElkR1	3	1.422	0.017	-4.377	0.018	0.614	0.019	32.5	2.6
ElkR2	1	-0.207	0.004	-3.846	0.007	0.606	0.044	34.4	3.8
WWR1	2	-0.945	0.000	-4.441	0.013	0.600	0.026	35.8	4.4
WWR2	1	-1.019	0.003	-4.471	0.008	0.607	0.039	34.2	3.3
Wayne Bb	2	-0.143	0.019	-4.216	0.009	0.594	0.017	37.3	3.1
918-52 1 B	1	0.397	0.006	-3.149	0.012	0.572	0.027	43.1	2.6
918-43.2 1 B	3	0.499	0.017	-3.370	0.072	0.585	0.011	39.5	1.6
918 52 B2	2	0.308	0.001	-3.327	0.027	0.580	0.020	41.1	3.6
918 43.2 B2a	2	0.302	0.008	-3.701	0.043	0.601	0.020	35.5	3.5
918 43.2 B	1	0.479	0.004	-3.432	0.007	0.581	0.033	40.6	3.0
918 43.2	1	0.506	0.015	-3.426	0.031	0.588	0.016	38.9	1.4
907.23F 1 B	1	-0.289	0.007	-3.863	0.017	0.564	0.040	45.3	3.8
906 23-30 T1	2	-0.372	0.008	-4.090	0.018	0.584	0.029	40.0	5.1
906 23-30 1 B	1	-0.194	0.007	-4.064	0.013	0.565	0.031	44.9	2.9
906 2 T	1	-0.292	0.014	-4.214	0.027	0.577	0.031	41.8	2.9
906 1 T	4	-0.240	0.013	-4.144	0.072	0.561	0.012	46.1	1.6
902.8 2 TC-S	1	1.041	0.012	-4.183	0.022	0.507	0.026	62.1	2.9
902.8 1 TC-G	1	-0.016	0.010	-4.782	0.020	0.533	0.038	54.1	3.9
SGH-W 43.0 T1	1	-0.524	0.003	-4.170	0.008	0.595	0.035	37.1	3.1
SGH-W-43.0 Cr1	1	-0.078	0.063	-4.267	0.082	0.586	0.069	39.4	6.1
SGH-W-43.0-B1	1	0.413	0.004	-4.878	0.007	0.585	0.030	39.7	2.7
SGH-W-42.2 R1	1	-0.589	0.003	-4.310	0.006	0.590	0.026	38.3	2.3
KY127B1	1	0.730	0.027	-4.712	0.060	0.587	0.036	39.0	3.2
KY127Bry1	1	0.090	0.018	-4.050	0.021	0.601	0.051	35.6	4.4
MCc-F-4.8-Bry1	1	-1.367	0.002	-4.444	0.004	0.570	0.043	43.6	4.0
Mol Isotelus b	2	-0.760	0.000	-4.901	0.005	0.605	0.015	34.6	2.6
MM1-Bb	3	-0.595	0.014	-4.627	0.016	0.586	0.017	39.5	2.5
HC-K T1	1	-1.007	0.002	-5.880	0.004	0.585	0.027	39.8	2.5
HC-K-18-B1	1	-0.175	0.003	-4.842	0.008	0.580	0.040	40.9	3.6
Dec B1	2	-0.275	0.003	-4.671	0.018	0.597	0.018	36.6	3.2
Dec B2	2	0.432	0.006	-4.871	0.025	0.601	0.025	35.7	4.3
Dec T1	2	-0.528	0.005	-5.135	0.029	0.590	0.018	38.3	3.2

Table S1: Source, type, locality, stratigraphic context, estimated age, δ13C, δ18O, Δ47, temperature, δ18Owater, textural alteration status, and trace metal data for samples referred to in text and SOM.

sample	$\delta^{18}O_{water}$ (VSMOW)	$\delta^{18}O_{water}$ stdev	textural alteration?	Sr ppm	Mn ppm	Fe ppm	PC1	taxon specific PC1
A1391b-31	-0.592	-	no	-	-	-	-	-
A1391b-31	-0.747	-	no	-	-	-	-	-
A1391b-06	-0.687	-	no	-	-	-	-	-
A1391b-06	-0.982	-	no	-	-	-	-	-
A1380b-30	-1.298	-	no	-	-	-	-	-
A1356a-37	-1.191	-	no	-	-	-	-	-
A1356a-07	0.833	-	no	-	-	-	-	-
A1356a-07	0.683	-	no	-	-	-	-	-
A-958-4 alt	3.266	-	yes	-	-	-	-	-
A-958-3	2.644	-	yes	-	-	-	-	-
A-958-2 alt	3.697	-	yes	-	-	-	-	-
A-958	3.955	-	yes	-	-	-	-	-
A 551 alt	4.079	-	yes	-	-	-	-	-
922-F-RC	3.285	0.428	yes	-	-	-	-	-
922 2 TC G	2.252	0.700	yes	458	147	547	2.15	
922 1 TC S	1.842	0.677	yes	418	76	267	1.22	
923-0.9-RC	2.283	0.501	no	467	160	219	1.60	2.78
916MF 3 RC	0.264	0.400	no	-	-	-	-	-
916MF 2 B	0.633	0.708	no	890	65	140	0.56	0.52
916 RC 2	-0.021	0.468	no	-	-	-	-	-
916 MF RC2	0.242	0.715	no	784	20	112	-0.40	-0.12
916 MF B 4	0.724	0.567	no	-	-	-	-	-
916 MF 1 B	1.652	0.589	no	814	41	198	0.48	0.56
916 Bc RC	1.386	0.457	yes	846	58	168	0.61	1.33
916 B SI	0.547	0.551	no	759	69	137	0.62	0.60
901 19 RC 2	0.766	0.492	no	704	22	64	-0.69	-0.45
Lbec F B	1.564	0.614	no	990	45	159	0.37	0.35
912.98 2 RC	1.452	0.544	no	804	42	108	0.10	0.64
912 .98 1B	1.869	0.326	no	780	80	101	0.52	0.39
911 2.1 RC	1.519	0.386	no	680	28	54	-0.62	-0.31
912.98 B2	2.704	0.524	no	980	61	162	0.60	0.60
901-15-RC1	0.910	0.440	no	-	-	-	-	-
901-12-RC3	2.039	0.485	no	580	45	120	0.27	0.88
901-12-RC2	2.330	0.324	no	684	27	61	-0.57	-0.26
901 12 TC	1.266	0.664	yes	679	36	104	-0.01	
901 12 RC 1	3.128	0.827	no	400	21	62	-0.65	-0.39
901 12 LRC	1.639	0.392	no	902	27	100	-0.29	0.08
901.11 1 TC	2.833	0.720	yes	329	365	541	2.84	
901 10 RC 2	2.213	0.317	no	672	19	69	-0.73	-0.53
901 10 RC 1	2.558	0.727	no	704	12	54	-1.23	-1.24
901 8.5 B	2.362	0.700	yes	-	-	-	-	-
912.8 B 2	3.255	0.775	no	-	-	-	-	-
912-.8 2 T	1.501	0.465	no	763	15	39	-1.30	-0.81
912 0.8 B	3.257	0.453	no	746	55	186	0.66	0.75
908 1 T	0.688	0.361	no	880	14	32	-1.50	-1.07
904.4 2 RC	2.691	0.375	no	308	46	166	0.60	1.31
904.25 1 B	3.570	0.270	yes	579	68	143	0.68	0.72
904 4.5 RC	1.669	0.528	no	897	13	47	-1.30	-1.32

Table S1: Source, type, locality, stratigraphic context, estimated age, δ13C, δ18O, Δ47, temperature, δ18Owater, textural alteration status, and trace metal data for samples referred to in text and SOM.

sample	$\delta^{18}O_{water}$ (VSMOW)	$\delta^{18}O_{water}$ stdev	textural alteration?	Sr ppm	Mn ppm	Fe ppm	PC1	taxon specific PC1
904 .4 B1	1.215	0.642	no	1100	14	40	-1.39	-1.99
904 .4 1RC	2.254	0.386	no	900	21	51	-0.91	-0.74
ElkR1	-0.559	0.512	no	762	36	51	-0.50	-0.12
ElkR2	0.334	0.741	no	742	20	59	-0.82	-0.63
WWR1	0.003	0.862	no	684	17	63	-0.88	-0.73
WWR2	-0.337	0.653	no	584	31	52	-0.55	-0.20
Wayne Bb	0.512	0.585	no	1252	17	37	-1.32	-1.96
918-52 1 B	2.647	0.470	yes	-	-	-	-	-
918-43.2 1 B	1.780	0.303	yes	-	-	-	-	-
918 52 B2	2.099	0.669	yes	772	49	205	0.64	0.75
918 43.2 B2a	0.687	0.681	no	-	-	-	-	-
918 43.2 B	1.911	0.565	yes	805	57	179	0.65	0.71
918 43.2	1.607	0.262	yes	-	-	-	-	-
907.23F 1 B	2.327	0.700	yes	505	98	185	1.13	1.30
906 23-30 T1	1.147	0.977	no	640	29	90	-0.25	0.46
906 23-30 1 B	2.060	0.535	no	860	39	169	0.33	0.34
906 2 T	1.350	0.536	no	566	28	77	-0.36	0.30
906 1 T	2.194	0.282	no	712	48	261	0.79	1.79
902.8 2 TC-S	4.852	0.477	yes	461	203	403	2.17	
902.8 1 TC-G	2.934	0.682	yes	649	108	224	1.28	
SGH-W 43.0 T1	0.512	0.594	no	477	18	98	-0.49	0.28
SGH-W-43.0 Cr1	0.855	1.178	no	-	-	-	-	-
SGH-W-43.0-B1	0.300	0.512	no	-	-	-	-	-
SGH-W-42.2 R1	0.599	0.443	no	-	-	-	-	-
KY127B1	0.335	0.603	no	997	47	38	-0.54	-1.10
KY127Bry1	0.358	0.849	no	-	-	-	-	-
MCc-F-4.8-Bry1	1.443	0.745	no	-	-	-	-	-
Mol Isotelus b	-0.687	0.511	no	477	18	98	-0.49	0.28
MM1-Bb	0.501	0.462	no	1160	22	71	-0.70	-1.07
HC-K T1	-0.701	0.463	no	-	-	-	-	-
HC-K-18-B1	0.542	0.680	no	-	-	-	-	-
Dec B1	-0.074	0.620	no	902	36	91	-0.14	-0.37
Dec B2	-0.452	0.829	no	997	47	38	-0.54	-1.10
Dec T1	-0.232	0.608	no	878	10	34	-1.70	-1.23

Supplemental references

S1. A. Achab, E. Asselin, A. Desrochers, J. F. Riva, C. Farley, *Geological Society of America Bulletin* **123**, 186 (2011).
S2. C. R. Barnes, *Bulletin of the British Museum. Natural History. Geology Series* **43**, 195 (1988).
S3. P. Copper, *Canadian Journal of Earth Sciences* **38**, 153 (Feb, 2001).
S4. A. Desrochers, C. Farley, A. Achab, E. Asselin, J. F. Riva, *Palaeogeography, Palaeoclimatology, Palaeoecology* **296**, 248 (2010).
S5. N. R. Emerson, J. A. Simo, C. W. Byers, J. Fournelle, *Palaeogeography, Palaeoclimatology, Palaeoecology* **210**, 215 (2004).
S6. J. Simo, N. R. Emerson, C. W. Byers, G. A. Ludvigson, *Geology [Geology]* **31**, 545 (2003).
S7. M. E. Patzkowsky, S. M. Holland, *Special Paper - Geological Society of America* **306**, 131 (1996).
S8. M. C. Pope, S. M. Holland, M. E. Patzkowsky, *Special Publication of the International Association of Sedimentologists* **41**, 255 (2009).
S9. C. E. Brett, T. J. Algeo, *Guidebook - Kentucky Geological Survey* **1, Series 12**, 34 (2001).
S10. S. M. Holland, M. E. Patzkowsky, *Special Paper - Geological Society of America* **306**, 117 (1996).
S11. C. R. Scotese, W. S. McKerrow, in *Advances in Ordovician Geology,* C. R. Barnes, S. H. Williams, Eds. (Geological Society of Canada, 1991), vol. Paper 90-9, pp. 271-282.
S12. L. R. M. Cocks, T. H. Torsvik, *Journal of the Geological Society* **159**, 631 (December 1, 2002, 2002).
S13. N. Pinet, P. Keating, D. Lavoie, P. Brouillette, *American Journal of Science* **310**, 89 (2010).
S14. N. Pinet, D. Lavoie, P. Keating, P. Brouillette, *Tectonophysics* **460**, 34 (2008).
S15. D. G. F. Long, *Canadian Journal of Earth* **44**, 413 (2007).
S16. S. Zhang, C. R. Barnes, *Palaeogeography, Palaeoclimatology, Palaeoecology* **180**, 5 (2002).
S17. D. G. F. Long, *Canadian Journal of Earth Sciences* **44**, 413 (2007).
S18. D. G. F. Long, P. Copper, *Canadian Journal of Earth Sciences* **24**, 1807 (1987).
S19. P. J. Brenchley *et al.*, *Geology* **22**, 295 (Apr, 1994).
S20. A. Delabroye, M. Vecoli, *Earth Science Reviews* **98**, 269 (2010).
S21. B. J. Witzke, R. C. Heathcote, E. A. Bettis, R. R. Anderson, R. J. Heathcote, *Field Trip Guidebook - Geological Society of Iowa* **63**, 39 (1997).
S22. O. E. Childs, *AAPG Bulletin* **69**, 173 (1985).
S23. S. Root, C. M. Onasch, *Tectonophysics* **305**, 205 (1999).
S24. R. Bertrand, *Canadian Journal of Earth* **27**, 731 (1990).
S25. L. Quinn *et al.*, *Canadian Journal of Earth* **41**, 587 (2004).
S26. B. R. Shaw, M. Etemadi, Anonymous, *AAPG Bulletin* **75**, 671 (1991).
S27. S. M. Bergstrom, S. Young, B. Schmitz, *Palaeogeography, Palaeoclimatology, Palaeoecology* **296,** 217 (2010).

S28. W. Buggisch *et al.*, *Geology* **38**, 327 (2010).
S29. S. M. Bergstrom, M. M. Saltzman, B. Schmitz, *Geological Magazine* **143**, 657 (2006).
S30. D. Kaljo, L. Hints, P. Mannick, J. Nolvak, *Estonian Journal of Earth Sciences* **57**, 197 (2008).
S31. P. Copper, D. G. F. Long, *Newsletters on Stratigraphy* **21**, 59 (1989).
S32. M. J. Melchin, *Lethaia* **41**, 155 (2008).
S33. A. Achab, E. Asselin, A. Desrochers, J. F. Riva, C. Farley, *Geological Society of America Bulletin* **123**, 186 (2011).
S34. P. I. McLaughlin, C. E. Brett, *AAPG Bulletin* **84**, 1389 (2000).
S35. P. I. McLaughlin, C. E. Brett, S. L. Taha McLaughlin, S. R. Cornell, *Palaeogeography, Palaeoclimatology, Palaeoecology* **210**, 267 (2004).
S36. T. Sami, A. Desrochers, *Sedimentology* **39**, 355 (1992).
S37. S. A. Young, M. R. Saltzman, W. I. Ausich, A. Desrochers, D. Kaljo, *Palaeogeography, Palaeoclimatology, Palaeoecology* **296,** 367 (2010).
S38. R. E. Came, *Nature* **449**, 198 (2007).
S39. I. S. Al-Aasm, J. Veizer, *Journal of Sedimentary Petrology* **52**, 1101 (1982).
S40. B. Wenzel, C. Lecuyer, M. Joachimski, *Geochimica et Cosmochimica Acta* **64**, 1859 (2000).
S41. R. van Geldern *et al.*, *Palaeogeography, Palaeoclimatology, Palaeoecology* **240**, 47 (2006).
S42. P. Ghosh, *Geochimica et Cosmochimica Acta* **70**, 1439 (2006).
S43. S.-T. Kim, J. R. O'Neil, *Geochimica et Cosmochimica Acta* **61**, 3461 (1997).
S44. S. M. Savin, *Annual Review of Earth and Planetary Sciences* **5**, (1977).
S45. D. P. Schrag *et al.*, *Quaternary Science Reviews* **21**, 331 (2002).
S46. K. Lambeck, Y. Yokoyama, P. Johnston, A. Purcell, *Earth and planetary science letters* **181**, 513 (2000).
S47. Y. Yokoyama, *Nature* **406**, 713 (2000).
S48. V. Masson-Delmotte *et al.*, *Journal of Climate* **21**, 3359 (2008).
S49. J. G. C. Walker, K. C. Lohmann, *Geophysical Research Letters* **16**, 263 (1989).
S50. R. K. Wanless, R. D. Stevens, *Geological Association of Canada Proceedings* **23**, 77 (1971).
S51. U. Brand, *Chemical Geology* **204**, 23 (2004).
S52. U. Brand, J. Veizer, *Journal of Sedimentary Research* **50**, 1219 (1981).
S53. U. Brand, *Chemical Geology* **40**, 167 (1983).
S54. I. S. Al-Aasm, J. Veizer, *Journal of Sedimentary Petrology* **56**, 763 (1986).
S55. G. A. Shields *et al.*, *Geochimica et Cosmochimica Acta* **67**, 2005 (2003).
S56. D. G. F. Long, *Palaeogeography, Palaeoclimatology, Palaeoecology* **104**, 49 (1993).
S57. D. Kaljo, L. Hints, T. Martma, J. Nılvak, *Chemical Geology* **175**, 49 (2001).
S58. J. D. Marshall, P. D. Middleton, *Journal of the Geological Society of London* **147**, 1 (1990).
S59. L. Hints *et al.*, *Estonian Journal of Earth Sciences* **59**, 1 (2010).
S60. H. Qing, J. Veizer, *Geochimica et Cosmochimica Acta* **58**, 4429 (1994).
S61. A. Prokoph, G. A. Shields, J. Veizer, *Earth Science Reviews [Earth Sci. Rev.]*. **87**, 3 (2008).

S62. G. A. Shields *et al.*, *Geochimica et Cosmochimica Acta* **67**, 2005 (Jun, 2003).
S63. J. n. Veizer *et al.*, *Chemical Geology* **161**, 59 (1999).
S64. A. K. Tripati *et al.*, *Geochimica et Cosmochimica Acta* **74**, 5697 (2010).
S65. U. Brand, *Chemical Geology* **32**, 17 (1981).
S66. J. E. Sorauf, *Journal of Paleontology* **51**, 150 (1977).
S67. J. E. Sorauf, *Bolotin de la Real Sociedad Espanola de Historia Natural* **92**, 77 (1997).
S68. G. E. Webb, J. E. Sorauf, *Geology* **30**, 415 (2002).
S69. A. K. Tripati, C. D. Roberts, R. A. Eagle, *Science* **326**, 1394 (December 4, 2009, 2009).
S70. R. J. Stouffer, S. Manabe, *Climate Dynamics* **20**, 759 (2003).
S71. A. K. Tripati *et al.*, *Paleoceanography* **18**, 1101 (2003).
S72. C. H. Lear, Y. Rosenthal, H. K. Coxall, P. A. Wilson, *Paleoceanography* **19**, 4015 (2004).
S73. IPCC, Ed., *Climate Change 2007: The Physical Science Basis. Contribution of Working Group I to the Fourth Assessment Report of the Intergovernmental Panel on Climate Change*, (Cambridge University Press, Cambridge, U.K., and New York, N.Y., 2007).
S74. V. Masson-Delmotte *et al.*, *Climate Dynamics* **26**, 513 (2006).
S75. M. M. Holland, C. M. Bitz, *Climate Dynamics* **21**, (2003).